Geophysical Journal International

Geophys. J. Int. (2026) **244,** 1–24
Advance Access publication 2025 December 13
Research Paper

https://doi.org/10.1093/gji/ggaf517

Automated detection of short-term slow slip events using GNSS data via change-point analysis

Yiming Ma,[1,2] Andreas Anastasiou[3] and Fabien Montiel[1]

[1]*Department of Mathematics and Statistics, University of Otago, Dunedin* 9016, *New Zealand.*
[2]*Department of Mathematical Sciences, Auckland University of Technology, Auckland* 1010, *New Zealand. E-mail: yiming.ma@aut.ac.nz*
[3]*Department of Mathematics and Statistics, University of Cyprus, Nicosia* 1678, *Cyprus.*

Accepted 2025 December 11. Received 2025 October 14; in original form 2025 December 11

SUMMARY

Inferring from the occurrence pattern of slow slip events (SSEs) the probability of triggering a damaging earthquake within the nearby velocity weakening portion of the plate interface is critical for hazard mitigation. Although robust methods exist to detect long-term SSEs consistently and efficiently, detecting short-term SSEs remains a challenge. In this study, we propose a novel statistical approach, called singular spectrum analysis isolate-detect (SSAID), for automatically estimating the start and end times of short-term SSEs in Global Navigation Satellite System (GNSS) data. The method recasts the problem of detecting SSEs as that of identifying change-points in a piecewise nonlinear signal. This is achieved by obscuring the deviation from piecewise-linearity in the underlying SSE signals using added noise. We verify its effectiveness on a range of synthetic SSE data with different noise levels, and demonstrate its superior performance compared to two existing methods. We illustrate its capability in detecting short-term SSEs in observed GNSS data from 36 stations in southwest Japan via the co-occurrence of non-volcanic tremors, hypothesis tests and fault estimation.

Key words: Satellite geodesy; Transient deformation; Time-series analysis; Earthquake ground motions; Episodic tremor and slip.

1 INTRODUCTION

Slow slip events (SSEs) are fault slips occurring at the subduction interface between tectonic plates. They are roughly categorized into short-term SSEs (in the order of days to weeks) and long-term SSEs (in the order of months to years) (K. Obara 2020). They constitute a type of slow earthquakes (H. Hirose *et al.* 1999; K. Obara & A. Kato 2016; K. Obara 2020). SSEs play a vital role in releasing stress along subduction interfaces. The associated episodic stress perturbations on the seismogenic zone have been linked to the occurrence of larger natural earthquakes (P. Segall *et al.* 2006; Y. Ito *et al.* 2013; N.M. Bartlow *et al.* 2014; M. Radiguet *et al.* 2016; N. Voss *et al.* 2018; Q. Bletery & J.M. Nocquet 2020). SSEs might also prevent the rupture of large earthquakes from propagating further along the subduction interface, while large earthquakes can also initiate SSEs in the nearby transition zone (H. Hirose *et al.* 2012; H. Yarai & S. Ozawa 2013; T. Nishikawa *et al.* 2019; L.M. Wallace 2020; T. Nishimura 2021). Here the transition zone refers to the area where SSEs occur along the subduction interface. Understanding the process governing SSEs could potentially help us forecast impending earthquakes, although the underlying geophysical mechanism for forming SSEs remains elusive (S. Mazzotti & J. Adams 2004; T.H. Jordan & L.M. Jones 2010; R.B. Lohman & J.R. Murray 2013; N.M. Beeler *et al.* 2014; K. Obara & A. Kato 2016; S. Barbot 2019; K. Obara 2020).

Detecting SSEs accurately could be the key to determine the mechanism generating SSEs and understand their connection to large earthquakes (M.J. Ikari *et al.* 2013; D.M. Saffer & L.M. Wallace 2015; S.W. Ozawa *et al.* 2019; T. Nishimura 2021). SSEs are generally recorded through geodetic measurements such as Global Navigation Satellite System (GNSS), tiltmeters and strainmeters. Among these, the Global Positioning System (GPS; one type of GNSS) network is the most popular way of recording ground movements with the intention of uncovering SSEs, because it is relatively inexpensive, easily accessible and sufficiently precise (T.I. Melbourne *et al.* 2005; E.F. Smith & J. Gomberg 2009; M. Vergnolle *et al.* 2010; Y. Jiang *et al.* 2012; O. Cavalié *et al.* 2013; X. He *et al.* 2017). Developing a robust method for detecting SSEs in GNSS data is crucial, despite the many challenges it presents (T. Nishimura *et al.* 2013; T. Nishimura 2014, 2021; B. Rousset *et al.* 2017; J. Haines *et al.* 2019; R. Takagi *et al.* 2019; T. Nishikawa *et al.* 2019; Y. Okada *et al.* 2022). For ease of presentation, we refer to GNSS data recording SSEs as SSE data thereafter.

Numerous methods have been proposed to detect the occurrence times of SSEs in GNSS data (hereafter referred to as SSE detections). The first group of approaches is based on Kalman filter of

state vectors, which model the recorded GNSS time-series as the sum of coherent signals from various sources and estimation errors (K.H. Ji & T.A. Herring 2013; R. Granat *et al.* 2013; R.B. Lohman & J.R. Murray 2013; D. Walwer *et al.* 2016). These existing approaches include Network Inversion Filter (P. Segall & M. Matthews 1997; P. Segall *et al.* 2000; J.J. McGuire & P. Segall 2003; S. Miyazaki *et al.* 2003), Monte Carlo Mixture Kalman Filter (J. Fukuda *et al.* 2004, 2008), Network Strain Filter (R. Ohtani *et al.* 2010) and further improvements on the above Kalman-filter-based methods (K.H. Ji & T.A. Herring 2013; B. Riel *et al.* 2014; J. Bedford & M. Bevis 2018). These methods aim to extract the SSE signal from noisy GNSS data, but they rely on different assumptions about the state vectors they estimate. However, these assumptions are debated because the underlying mechanisms that govern SSEs are not yet fully understood (K. Obara & A. Kato 2016; K. Obara 2020).

Another group of approaches consists of estimating the time evolution of the slip distribution on the fault by inverting the recorded GNSS data at different sites, so that the occurrence times of SSEs can be simultaneously estimated (R. McCaffrey 2009; N.M. Bartlow *et al.* 2014; C.A. Williams & L.M. Wallace 2015; L.M. Wallace *et al.* 2017, 2018). One commonly used tool for such detection is TDEFNODE, which is a nonlinear time-dependent inversion code (R. McCaffrey 2009). This tool utilizes simulated annealing to downhill simplex minimization, which has been applied to invert various recorded GNSS data for detecting SSEs. Two free parameters in this method are the occurrence times and the associated amplitude of SSEs (R. McCaffrey 2009). TDEFNODE needs *a priori* information on the functional form (e.g. exponential or Gaussian) of the temporal evolution of SSEs on the fault. However, the selection of a suitable form remains enigmatic, and is generally determined by trial tests (L.M. Wallace *et al.* 2017). In addition, the geometry of the subduction zone must be known to use TDEFNODE, thus its application is affected by the availability of geometrical knowledge in the observed data.

Singular spectrum analysis (SSA), a univariate time-series analysis method (M. Ghil *et al.* 2002), can remedy this latter shortcoming. SSA is designed to extract information from noisy time-series and thus, provides insight into the underlying dynamics (M. Ghil *et al.* 2002). The key feature of this method is that it does not need any *a priori* knowledge of the underlying pure signal, and the trends obtained in this way are not necessarily linear (M. Ghil *et al.* 2002; Q. Chen *et al.* 2013; K. Ji *et al.* 2024; W. Tan *et al.* 2024). SSA typically decomposes the noisy data into reconstructed components (RCs). These RCs are sorted in a descending order according to their corresponding eigenvalues, which denote their proportions of the total variance of the original data. Low-order RCs in the queue are regarded as effective signals related to the underlying dynamics, while high-order RCs are taken as noise, and are typically discarded. This is the common way to extract pure SSEs from noisy data by SSA. To determine a threshold between pure signal RCs and noise RCs is relatively subjective. When the signal-to-noise ratio (SNR) is low, SSA normally fails to distinguish signal from noise. Q. Chen *et al.* (2013) demonstrated that SSA is a viable and complementary tool for extracting modulated oscillations from GNSS time-series.

D. Walwer *et al.* (2016) introduced a more powerful form of SSA, Multichannel Singular Spectrum Analysis (M-SSA), to detect SSEs. M-SSA can simultaneously make use of the spatial and temporal correlations to explore the spatiotemporal variability of GNSS data. In their approach, M-SSA was primarily used to remove seasonal components, yielding time-series that contained a mixture of SSE signals and noise. The occurrence times of SSEs was then identified visually. At each time-step, displacement was modelled as the sum of a residual inter-SSE trend and a hyperbolic tangent function representing the SSE. While M-SSA effectively isolated time-series where SSEs were embedded in noise, the study did not include an automated approach for determining SSE times, so a follow-up detection to determine the start and end times of SSEs is needed. In addition, the size of the lag covariance matrix in M-SSA also grows rapidly with the size of the GNSS network considered, leading to computational issues for large-scale networks. M-SSA cannot operate on a single data basis, which limits its applicability to cases where the signals lack spatial coherence, for example, when there are not enough GNSS stations, or the stations are too close to each other. Relative strength index (RSI), a single-station technique from the stock market (B.W. Crowell *et al.* 2016), is able to solve all the aforementioned issues, but it only applies to long-term SSEs.

Compared to long-term SSEs, the duration and recurrence interval of short-term SSEs are much smaller, in the order of several days or weeks. The amplitude change in the GNSS data caused by a short-term SSE is also relatively small. It can be close to, or even lower than, the background noise, so most short-term SSEs remain undetected (T. Nishimura 2021; K. Yano & M. Kano 2022). Therefore, more urgent efforts should be devoted to rapid automated methods for detecting short-term SSEs (H. Hirose & T. Kimura 2020; K. Obara 2020; Y. Okada *et al.* 2022), which is the focus of this study. Linear regression, combined with Akaike's Information Criterion (AIC), is widely used to detect short-term SSEs for large-scale GNSS networks (T. Nishimura *et al.* 2013; T. Nishimura 2014, 2021; Y. Okada *et al.* 2022). This method fits linear functions with and without an offset, and then uses AIC to judge which function is a better fit considering a number of free parameters. In this method, the length of the designed sliding window and the user-defined detection threshold determine the detection accuracy. In practice, it is hard to select reasonable values for these subjective parameters (T. Nishimura *et al.* 2013; K. Yano & M. Kano 2022). A new method developed by K. Yano & M. Kano (2022) can overcome this deficiency, approximating SSE data as piecewise-linear signals by using l_1 trend filtering combined with Mallows' C_p. The knots in the fitted piecewise-linear signal are then taken as the occurrence times of SSEs. The applications to both synthetic and observed SSE data demonstrated that this method obtained better performance than the linear regression method. However, it is not clear that the assumption that SSE data can be regarded as piecewise-linear signals with the knots being the occurrence times of SSEs is reasonable, since the specific form of the underlying SSE signal remains unknown (K. Obara & A. Kato 2016; K. Obara 2020).

In this study, we develop a new method, called singular spectrum analysis isolate-detect (SSAID), to automatically detect the start and end times of short-term SSEs in GNSS data. Our method regards the detection of short-term SSEs in GNSS data as a problem of detecting change-points in piecewise nonlinear signals, in which the start and end times of SSEs are change-points to be detected. The prominent advantage of SSAID is that it does not require prior knowledge of the exact form of the underlying SSE signal. Rather than attempting to capture the exact structure of SSE signals, SSAID aims to mask the deviations of the SSE signal's piecewise-nonlinear structure from the piecewise-linear form so that established change-point detection techniques developed for piecewise-linear signals can be used to detect SSEs. This is done by (i) decomposing the noisy SSE data into spectral components through SSA (M. Ghil *et al.* 2002) and reconstructing these components into new noisy data signals; (ii) adding noise to these reconstructed signals and (iii) conducting the detection by the Isolate-Detect (ID; A. Anastasiou & P. Fryzlewicz, 2022) algorithm. We conduct a range of simulations to evaluate the

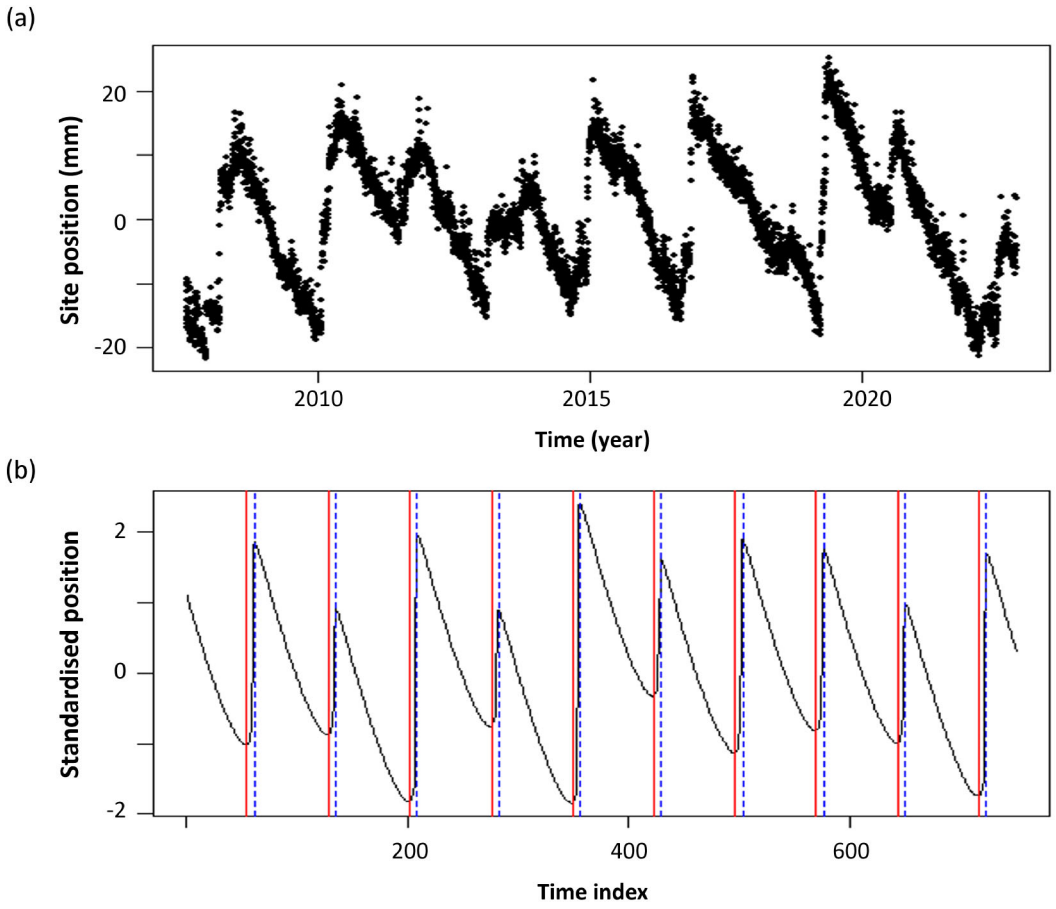

Figure 1. (a) Observed SSE data recorded by the east component of a GNSS station (MAHI), in the Hikurangi subduction zone, New Zealand; (b) Synthetic SSE data with 10 SSEs in a two-year period, which are simulated by a deterministic subduction slip model (see the supplement). Solid vertical lines (red): the start times of SSEs; dotted vertical lines (blue): the end times of SSEs.

detection performance of SSAID using both simulated and observed SSE data.

In Section 2, we introduce the method SSAID along with some assumptions. Additional methodological details are given in the appendix. In Section 3, we show results of applying SSAID to a range of simulated SSE data and compare the results with two existing detection methods (i.e. linear regression with AIC; and l_1 trend filtering). In Section 4, we introduce the observed SSE data in southwest Japan and the associated data processing procedures. In Section 5, we demonstrate our method's capability in detecting short-term SSEs in observed GNSS data introduced in Section 4. The validity of the detected change-points as actual SSEs is assessed using the same approach as K. Yano & M. Kano (2022), that is, correlation with tremors, hypothesis testing and fault estimation. Discussions and conclusions are in Section 6.

2 METHOD

We propose a new method to detect change-points in univariate time-series with continuous, piecewise nonlinear structure. Here, change-points refer to the times at which the pattern of the underlying dynamics (i.e. pure signal) changes from one state to a different one. Fig. 1(a) shows an example of observed SSE data from the Hikurangi subduction zone, New Zealand. In periods with no SSEs, the overall trend of the signal is linear and decreasing. The trend is then redirected to a different state (increasing here) when an SSE starts. Once the SSE ends, the trend reverses back to its original linear decreasing state. The start and end times of SSEs can therefore be regarded as change-points in GNSS data. Our method, called Singular Spectrum Analysis Isolate Detect (SSAID), seeks to detect the start and end times of SSEs in noisy GNSS data without prior knowledge of the underlying structure of the signal. Note that the linear trend of the presented SSE data has been removed, which is not necessarily equivalent to the true secular plate motion at a given GNSS site. Here, we only summarize its underlying assumptions and main features. A full exposition of the methodology can be found in the appendix and the supplement (see Section S8 in the supplement).

Let us assume that the deviation in the pure SSE signal from a piecewise-linear function can be obscured by noise as long as the noise level is within a suitable range, so that SSE data with this range of noise levels can simply be taken as piecewise-linear signals. If the condition is met, an existing change-point detection method specifically designed for piecewise-linear signals can be directly applied to detect change-points in SSE data. If the condition is not met, the existing change-point detection method for piecewise-linear signals will overestimate the number of change-points for low noise levels and underestimate them for high noise levels. This assumption was validated using numerical tests (see Section S3 in the supplement), in which various change-point detection methods for piecewise-linear signals were shown to successfully detect change-points after different levels of Gaussian noise were added to the signal. Of all

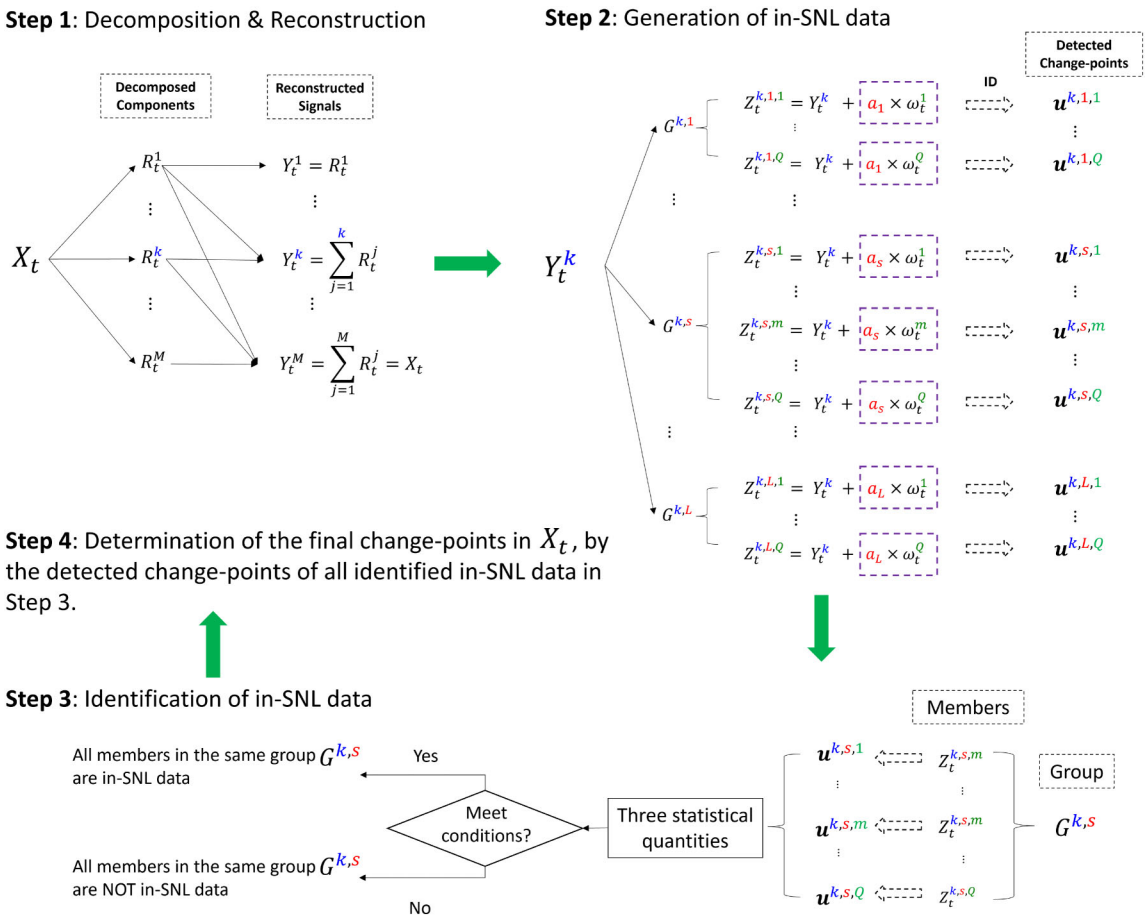

Figure 2. The full workflow of SSAID showing how to find the change-points in the noisy time-series X_t step by step.

the methods considered, Isolate-Detect (ID; A. Anastasiou & P. Fryzlewicz, 2022) showed the best performance and was therefore selected for application to SSE data. The noise level within a suitable range, that is, allowing successful change-point detection, is referred to as a suitable noise level (SNL). It describes the range of noise levels for which the deviation of SSE signal structures from piecewise linearity is sufficiently obscured so that an existing change-point detection method can be directly applied to detect change-points in SSE data and achieve a success rate exceeding 50 per cent. The existence of SNLs is confirmed through extensive numerical tests (see Section S3 and Fig. S9 in the supplement).

For the remainder of this paper, we define a successful *cumulative detection* when two conditions are met: (1) the number of estimated change-points is exactly the number of true change-points and (2) the root mean squared error (RMSE) of the detected change-point locations is less than a pre-defined threshold value v, here $v = 3$ d (see Section S3 and Fig. S8 in the supplement for a justification).

As the SNL varies with signal types (see Fig. S9 in the supplement), it is not possible to pre-determine if the raw data has an SNL. By decomposing the raw data and systematically adding Gaussian noise, SSAID generates new time-series with SNL (referred to as in-SNL data), greatly improving the probability of successful change-point detection.

SSAID contains four main steps: (1) decomposing and reconstructing the signal using SSA; (2) adding Gaussian noise with different noise levels to reconstructed signals; (3) detecting change-point candidates in SSE data via the Isolate-Detect algorithm (A. Anastasiou & P. Fryzlewicz 2022) and identifying in-SNL data and (4) determining the final change-points to best characterize the start and end times of SSEs. Fig. 2 summarizes the workflow of the method. Brief descriptions for each step are provided below. The reader is referred to the appendix for a full exposition of the method.

(i) **Signal decomposition and reconstruction:** We decompose the input data X_t (see eq. 1) into M components R_t^j $(j = 1, \cdots, M)$ using SSA, sorted by their correlation with the underlying dynamics. Components with smaller j values are important for the signal, while larger j values mostly contain noise. We then reconstruct M new data sequences in the form of cumulative sums: $Y_t^k = \sum_{j=1}^{k} R_t^j$ $(k = 1, \cdots, M)$. As k increases, Y_t^k gets closer to X_t, with $Y_t^M = X_t$. Examples of applying SSA to decompose and reconstruct simulated and observed SSE data are provided in Figs S13–S14 in the supplement.

(ii) **Generation of in-SNL data:** We add Gaussian noise with different noise levels to each reconstructed data Y_t^k, defined as $Z_t^{k,s,m} = Y_t^k + a_s \omega_t^m$ for $s = 1, \cdots, L$ and $m = 1, \cdots, Q$, where ω_t^m are independent, random variables sampled from the standard normal distribution. Here, a_s represents the noise level, and L and Q denote the number of noise levels and realizations considered, respectively. This step ensures the presence of in-SNL data among these newly created $Z_t^{k,s,m}$ time-series. For simplicity, we refer to the set of all realizations $G^{k,s} = \{Z_t^{k,s,1}, \cdots, Z_t^{k,s,Q}\}$ as a group for presentation in the next step.

(iii) **Identification of in-SNL data:** We apply the ID methodology to detect change-points $\mathbf{u}^{k,s,m}$ for each newly created time-series $Z_t^{k,s,m}$. Subsequently, we compute three statistical quantities for

$\mathbf{u}^{k,s,m}$ in each group and apply specific conditions (see appendix for details), so that if these conditions are satisfied, all realizations $Z_t^{k,s,m}$ within the same group are classified as in-SNL data; otherwise, they are classified as not in-SNL data.

(iv) **Determination of change-points in X_t:** We identify change-points in the input data X_t through a majority voting rule based on the identified in-SNL data. This process involves two sub-steps: (1) determining the number of change-points in X_t, denoted as $\hat{N}_X$, using the counts of the estimated change-points from the identified in-SNL data; and (2) locating the change-points by finding the mode and the average of each column in a matrix. This matrix comprises the selected $\mathbf{u}^{k,s,m}$, with each $\mathbf{u}^{k,s,m}$ containing the locations of the $\hat{N}_X$ change-points.

3 TESTS ON SYNTHETIC DATA

We now evaluate the detection performance of our method for a range of simulated noisy SSE data X_t, which are generated in the following form,

$$X_t = f_t + r_t, \quad (t = 1, \cdots, T), \tag{1}$$

where T is the length of the noisy data, f_t is the simulated pure SSE data and r_t denotes the noise model contained in X_t. Since the underlying mechanisms that govern SSEs are not yet fully understood (K. Obara & A. Kato 2016; K. Obara 2020), the exact structure of SSE signals remains uncertain, making it impossible to generate synthetic SSEs that perfectly reproduce real ones. Previous studies have typically modelled SSEs using simple analytical piecewise-nonlinear functions, such as logistic or arctangent forms (D. Walwer *et al.* 2016; J. Bedford & M. Bevis 2018; F. Donoso *et al.* 2023; X. Xue & J.T. Freymueller 2023). However, these simplifications cannot fully capture the complex dynamics of SSEs, particularly their interactions with other parts of the subduction zone. Therefore, in our synthetic tests, we employ both model-generated SSEs and analytical-function SSEs to thoroughly evaluate the detection performance of our method. These tests are organized into three groups, each containing 10 simulated SSEs, for a total of 20 true change-points (i.e. $N_0 = 20$). Each group includes multiple time-series generated with different noise realizations, allowing a comprehensive evaluation of the method's performance under varying conditions. The underlying SSE signals differ across groups. The first group uses SSEs generated from a deterministic subduction slip model [Fig. 1(b), see Section S2 in the supplement], providing a realistic evolution of SSEs and testing robustness across noise levels from low to very high, rather than validation against specific data sets. The second and third groups employ a logistic function to simulate SSE signals analytically (see Section S6 in the supplement), offering greater flexibility in controlling SSE amplitudes, and incorporate a realistic noise model simulated by the FAKENET package (D.C. Agnew 2013). In the second group, the 10 SSEs have irregular amplitudes, with some events changing sign, to assess how amplitude variability and sign changes affect detection performance. To better reflect real scenarios, where SSE amplitudes often evolve more systematically, the third group replaces the irregular SSEs of the second group with a regular pattern. This group is designed to investigate how the amplitude of regular SSEs affects detection performance.

The detection performance of SSAID is controlled by three parameters: the number of SSA components M, the number of realizations Q, and the highest level of added noise levels in percentage L. The selection of the lag-window size M (i.e. the number of decomposed components) is a well-recognized and actively researched topic in the field of SSA. While various studies have proposed guidelines, it remains a methodological challenge to define a universally optimal value for M, particularly in real-world applications (R. Vautard *et al.* 1992; M. Ghil *et al.* 2002; Q. Chen *et al.* 2013; D. Walwer *et al.* 2016; K. Ji *et al.* 2024; W. Tan *et al.* 2024). In our study, the recurrence period of SSEs is roughly two months within a two-year daily position time-series. Therefore, based on empirical insights from previous studies and considering computational constraints, we selected $M = 100$ as an appropriate window length for our analysis. Parameters L and Q should be set to sufficiently high values. A larger L ensures the presence of in-SNL data, while a larger Q enhances the detection success rate (see details in Appendix A2). However, it is crucial to impose upper limits on both L and Q to manage computing costs, as the computational demands increase significantly with higher values of these parameters. Based on numerical studies (see more details about the selection of these parameters in Section S5 in the supplement), we choose the default values $M = 100$, $L = 80$ and $Q = 40$ to achieve good performance.

3.1 Group 1 tests: model-simulated SSEs with varying noise levels

We begin with scenarios in which the pure SSE signal [f_t in eq. (1); see Fig. 1(b)] is simulated using a deterministic subduction slip model (see Section S2 in the supplement). The noise model is set as white noise, represented by:

$$r_t = C_{\text{wn}} \times \epsilon_t, \quad (t = 1, \ldots, T), \tag{2}$$

where ϵ_t are independent Gaussian random variables with mean zero and variance one. The noise level C_{wn}, representing the standard deviation, varies from 1 per cent to 100 per cent in 1 per cent increments. It corresponds to the ratio of the noise's standard deviation to the signal's standard deviation (equal to 1 after Z-score normalization). Figs 3(c) and (d) illustrate two examples of simulated SSE time-series with different noise levels. Ideally, if the detection is perfectly accurate, the blue solid lines and the red dotted lines would align exactly. However, in practice, the results from all detection methods are prone to errors due to the presence of noise, thus some offsets between the detected and actual change-points are to be expected. If the offset is smaller than a pre-defined threshold ($\upsilon = 3$ in our study), the change-point is considered successfully detected [as reflected in the R_{sd} results; see panel (b)]. Otherwise, it is classified as a false detection. We create 100 independent sequences of ϵ_t and apply each to 100 noise levels, resulting in a total of 100×100 noisy time-series X_t of length T. The pure SSE signal f_t is standardized using Z-score normalization (mean zero, variance one) to ensure its amplitude changes are comparable to those introduced by the white noise across all noise levels.

3.1.1 Detection results

Fig. 3(a) shows the error between the number of estimated change-points $\hat{N}_X$ by SSAID and the number of true change-points N_0 for each noisy time-series. We can observe that SSAID correctly estimates the number of true change-points in over 70 per cent of all cases analysed. In particular, the number of estimated change-points is correct for all the cases with noise levels lower than 25 per cent [see green box in Fig. 3(a)]. To quantify the detection performance

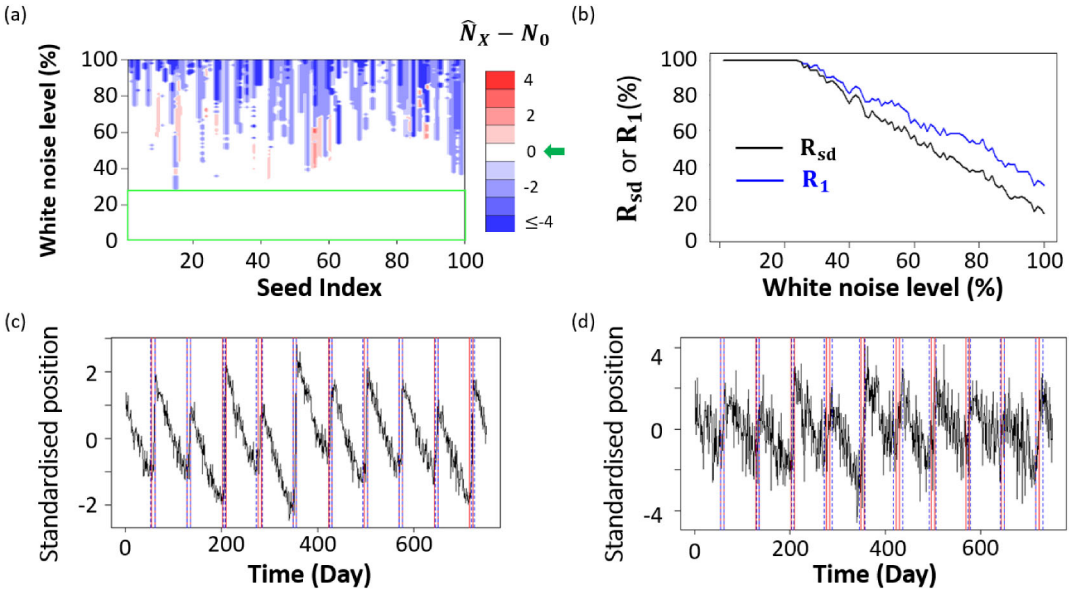

Figure 3. (a) The error between the number of estimated change-points $\hat{N}_X$ by SSAID and the number of true change-points N_0 in each simulated noisy data. The error of zero is highlighted by a green arrow in the colour bar. (b) The percentage R_1 and R_{sd} [see definitions in eq. (3)] as a function of white noise level C_{wn}, calculated from 100 seeds. The locations of the detected change-points in two simulation examples with different noise levels are shown in (c) $C_{wn} = 25$ per cent; (d) $C_{wn} = 100$ per cent. Dotted vertical lines (blue): estimated change-points by SSAID; solid vertical lines (red): true change-points.

of SSAID, we define

$$R_{sd} = \frac{\alpha}{\xi} \quad \text{and} \quad R_1 = \frac{\beta}{\xi}, \tag{3}$$

where ξ is the number of simulations for each noise level (i.e. $\xi = 100$ here), α is the number of successful cumulative detections, as defined in Section 2), and β is the number of cumulative detections for which the number of estimated change-points, $\hat{N}_X$, is equal to the number of true change-points N_0 (i.e. $\hat{N}_X = N_0 = 20$ here), but not with the RMSE requirements imposed on α.

Fig. 3(b) shows that R_{sd} and R_1 are different. They are both 100 per cent when $C_{wn} < 25$ per cent, and then decrease with increasing C_{wn} values. This implies that the successful cumulative detection rate is higher when the GNSS data have a smaller noise level, with 100 per cent success rate if the noise level is less than 25 per cent. R_{sd} decreases faster than R_1 when C_{wn} increases, indicating that the accuracy of the detected change-point locations fades with increasing C_{wn} values. Fig. 3(c) demonstrates the high accuracy of the change-points detected using our method for data with a low noise level. Fig. 3(d) shows a simulated time-series with high noise level ($C_{wn} = 100$ per cent) for which cumulative detection was unsuccessful (correct number of change-points, but too large error). Even though the locations of some detected change-points are not as accurate as for lower noise levels, SSAID remains relatively performant in terms of both the estimated number of change-points and their locations.

3.1.2 Comparison with two existing methods

We now compare the detection performance of SSAID with two existing detection methods for short-term SSEs. The first one is linear regression combined with AIC proposed by T. Nishimura *et al.* (2013), which has been widely applied in different areas (T. Nishimura *et al.* 2013; T. Nishimura 2014, 2021; Y. Okada *et al.* 2022). This method (1) uses a sliding window with a fixed width; (2) fits a linear model to the data in the window; (3) divides the data in the window into equal halves and fits a linear model to each half and (4) calculates the AIC difference (i.e. ΔAIC) between the single linear model and the two-line model at the middle point of the window. If that midpoint is a change-point, for example, the start- or end-point of an SSE, the two-line model fits the observational data better than a single linear model, thus resulting in a negative ΔAIC. As a negative ΔAIC does not always correspond to change-points in SSE signals, one must specify an appropriate threshold, denoted by ζ, in order to detect change-points of SSEs. If ΔAIC is lower than ζ, its corresponding time is regarded as a change-point. The detection performance of the linear regression approach is mainly controlled by the length of the sliding window and the specified threshold ζ, however, and selecting appropriate values for the two parameters is subjective (T. Nishimura *et al.* 2013; T. Nishimura 2021).

In our comparison tests, we first take a sliding time window of 180 d, which is consistent with that of T. Nishimura *et al.* (2013), to calculate ΔAIC for each data point of the simulated SSE data in Figs 3(c) and (d). Figs 4(a) and (b) show ΔAIC values across the time-series with three threshold values: $\zeta = -10, -20$ and -30 (later referred to as low, medium and high, respectively, in absolute value). We observe that the change-points at both ends of the simulated data cannot be detected regardless of the selected threshold due to the excessive length of the sliding window. This demonstrates that a smaller sliding window is needed (K. Yano & M. Kano 2022). We then decrease the sliding window to 15 d to calculate ΔAIC for each data point again, and we have a much shorter blinded interval of 7 d at both ends of the simulated period. In Figs 4(c) and (d), we also observe that none of the detection thresholds considered succeeds in finding all the true change-points accurately. When ζ is too low, only the most significant SSEs can be detected, while for larger ζ, the detection generally overestimates the number of change-points. The selection of the threshold value depends on the signal itself, making it impossible to detect all the change-points in multiple time-series or even within a single time-series by using a single threshold.

We then apply the method proposed by K. Yano & M. Kano (2022) to the synthetic data considered in Fig. 3 The method (1) applies l_1

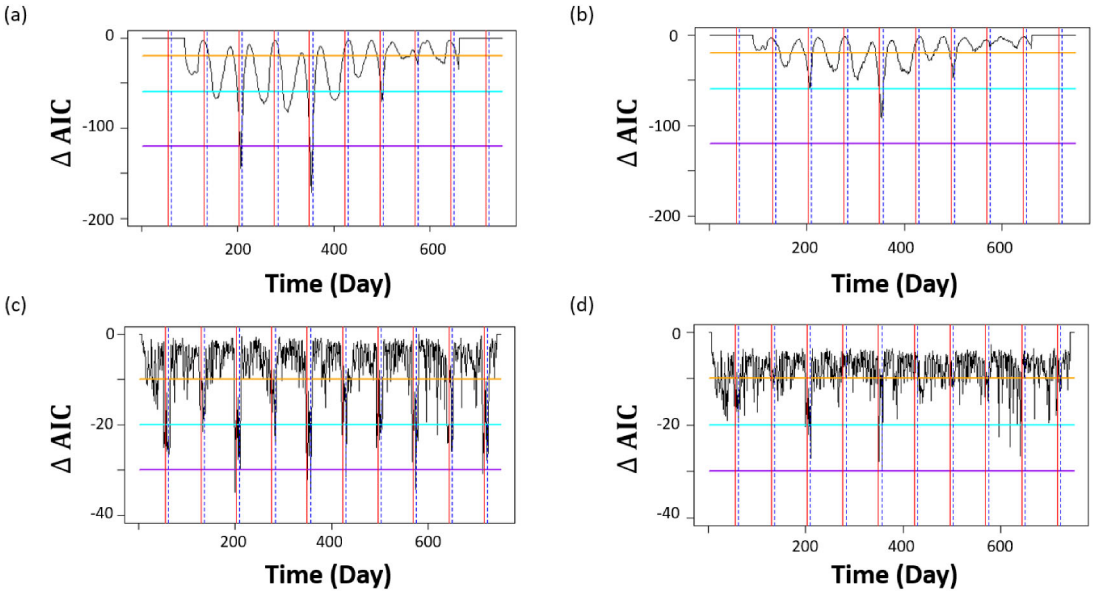

Figure 4. The calculated ΔAIC for different noisy data with different sliding windows. Panels (a) and (b) are plotted for the noisy data shown in Figs 3(c) and (d) with a sliding window of 180 d, respectively. While panels (c) and (d) are the same as (a) and (b) but with a sliding window of 15 d. Horizontal solid lines are associated with different thresholds to identify change-points of SSEs: high threshold (-30, purple); medium threshold (-20, cyan); low threshold (-10, orange). The intersections between horizontal lines and ΔAIC curve are considered as change-points. Solid vertical lines (red): start times of SSEs; dotted vertical lines (blue): end times of SSEs.

trend filtering to the raw data $X_i (i = 1, \cdots, T)$ with a range of hyperparameters λ; (2) obtains a fitted piecewise-linear signal $\hat{X}_t (t = 1, \cdots, T)$ for each λ; (3) calculates the associated Mallows' C_p for each λ, which is defined by $\sum_{t=1}^{T}(X_t - \hat{X}_t)^2/\hat{\sigma}_s^2 + N_{\text{knots}} + 2$, with σ_s^2 and N_{knots} representing the noise variance of X_t and the number of knots in $\hat{X}_t$, respectively; (4) chooses the one with the minimum Mallows' C_p as the best piecewise-linear approximation to characterize the raw data and (5) takes the knots of the chosen piecewise-linear model as the occurrence times of SSEs. Fig. S15 in the supplement illustrates an example of determining a suitable λ value for a noisy time-series. This method is similar to other change-point detection methods for piecewise-linear signals, for which we have demonstrated that they cannot be directly applied to detect SSEs in GNSS data (see Section S3 in supplement). Figs 5(a) and (b) show that in most cases l_1 trend filtering overestimates the number of change-points in simulated SSE data and its associated successful cumulative detection ratio R_{sd} for each noise level is much lower than that of SSAID, regardless of the noise level.

At its core, the method of l_1 trend filtering is equivalent to CPD designed for piecewise-linear signals, and therefore is not well suited for identifying change-points in piecewise-nonlinear signals such as those associated with SSEs. This limitation is consistent with our test results presented in the supplement (see Section S3), where we evaluated five commonly used change-point detection methods developed for piecewise linear signals. The results confirm that these methods are not directly applicable to SSE detection. All of the tested methods, including our own, operate on single-station time-series and do not incorporate spatial information. However, our method achieves superior detection performance with significantly fewer false positives. In contrast, the method of l_1 trend filtering yields a large number of false positives [see Figs 5(c) and (d)]. This advantage stems from our design, which aims to generate noisy time-series with SNLs before applying SSE detection, rather than directly apply the CPD detection methods to detect SSEs. Under SNLs, the distinction between piecewise linear and piecewise nonlinear signals becomes less apparent, allowing existing methods to better satisfy their model assumptions. As a result, our method achieves high detection accuracy with significantly fewer false detections.

We now compare the performance of the aforementioned methods quantitatively by calculating the total number of detected change-points across all considered scenarios (i.e. all noise levels and all seeds), as well as the counts of correct and false detections. An estimated change-point is considered correct if its error is no more than 3 d from any true change-point location (as previously justified); otherwise, it is regarded as false. Both the total number of detected change-points and the number of correctly detected change-points are expected to be $20 \times 10\,000$. In Fig. 6(a), we can see that the method SSAID aligns well with the expected values, exhibiting a satisfactory total number of detected change-points and a considerable number of correct detections, with minimal false detections. However, when using the l_1 trend filtering method, we observe that the total number of detected change-points is about twice the expected value, indicating a severe overdetection issue. The results obtained with the method of linear regression with ΔAIC underscore the significant influence of the chosen threshold ζ on the success of detection. Setting the threshold to a low value results in a large number of false detections. Conversely, choosing the threshold ζ to a medium value [see -20 in Fig. 6(a)] can significantly reduce false detections, but leads to a notable overestimation of true change-points. Further changing ζ to a higher threshold level causes the majority of detections to miss the true change-points.

We also analyse the detection frequency for each true change-point in the simulated data, which we should expect to be 10 000. Fig. 6 (b) shows that the detection results obtained by SSAID exhibit slight oscillations around the expected values, indicating greater stability compared to the other methods. We conducted further analysis on the histograms of the detected change-points for all the simulated noisy SSE data from all the different seeds and noise levels by these detection methods (see Figs S16–S17 in the

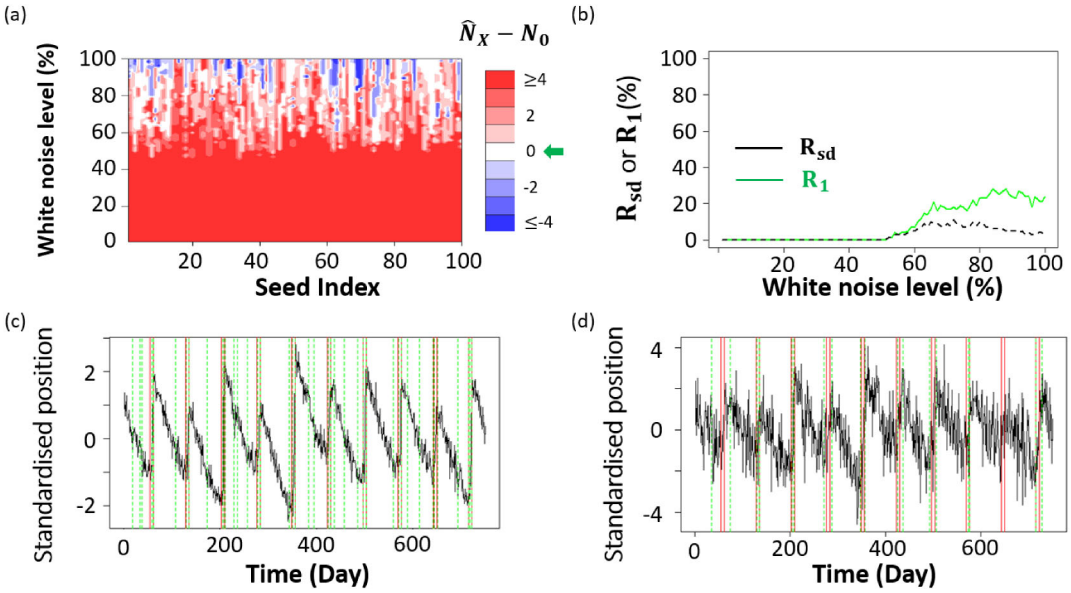

Figure 5. Same as Fig. 3 but using l_1 trend filtering to detect change-points in simulated SSE data.

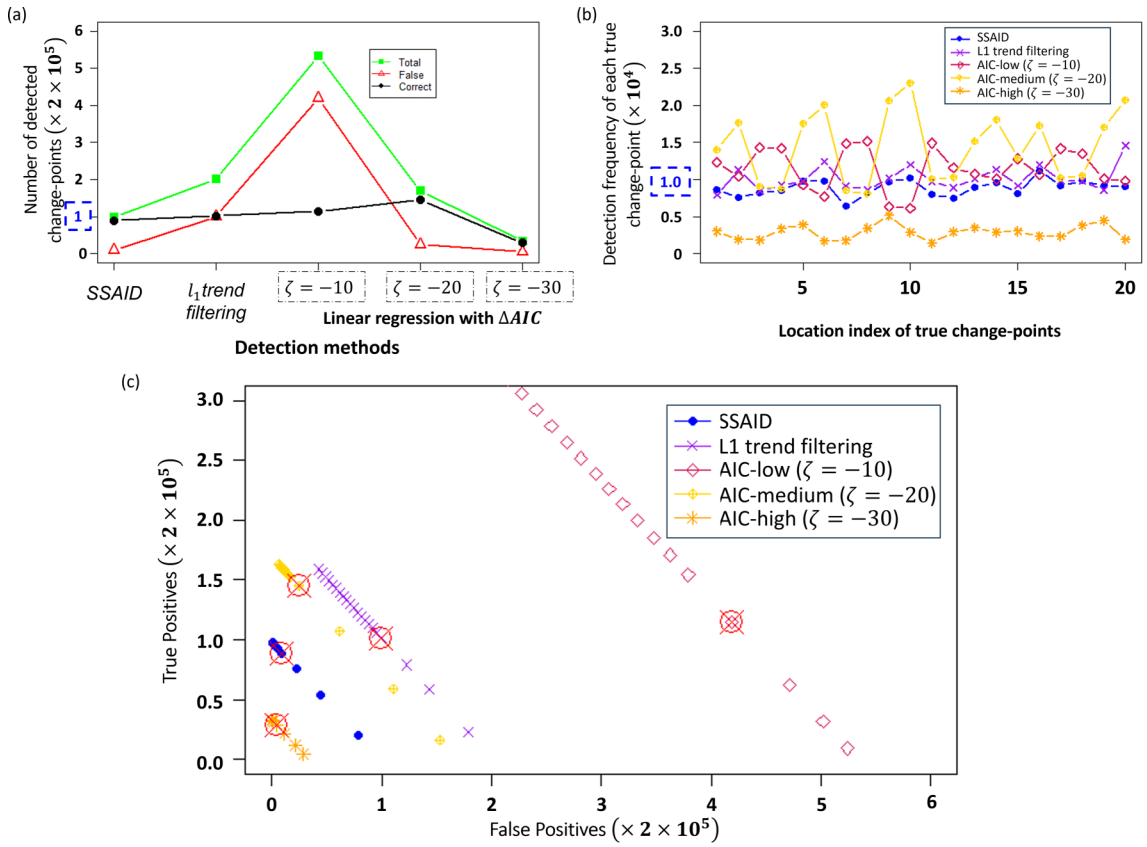

Figure 6. (a) Number of different detected change-points by various methods; (b) detection frequency of each true change-points by different methods. The total number of detected change-points and the number of correctly detected change-points are expected to be 20 × 10 000, while the expected detection frequency of each true change-point is 10 000. These expected values are highlighted by the blue dotted boxes. (c) Plots of false-true positives for each detection method with different thresholds of pre-defined acceptable error, ranging from 1 to 20 d. The dots marked with crossed circles (red) correspond to an acceptable error of 3 d.

supplement). The results indicate that most SSAID detections tend to converge to accurate locations with minimal errors, while the other methods, despite exhibiting similar behaviours, either suffer from a higher number of false detections and larger errors, or miss the majority of true change-points. This further demonstrates the superior detection performance of SSAID.

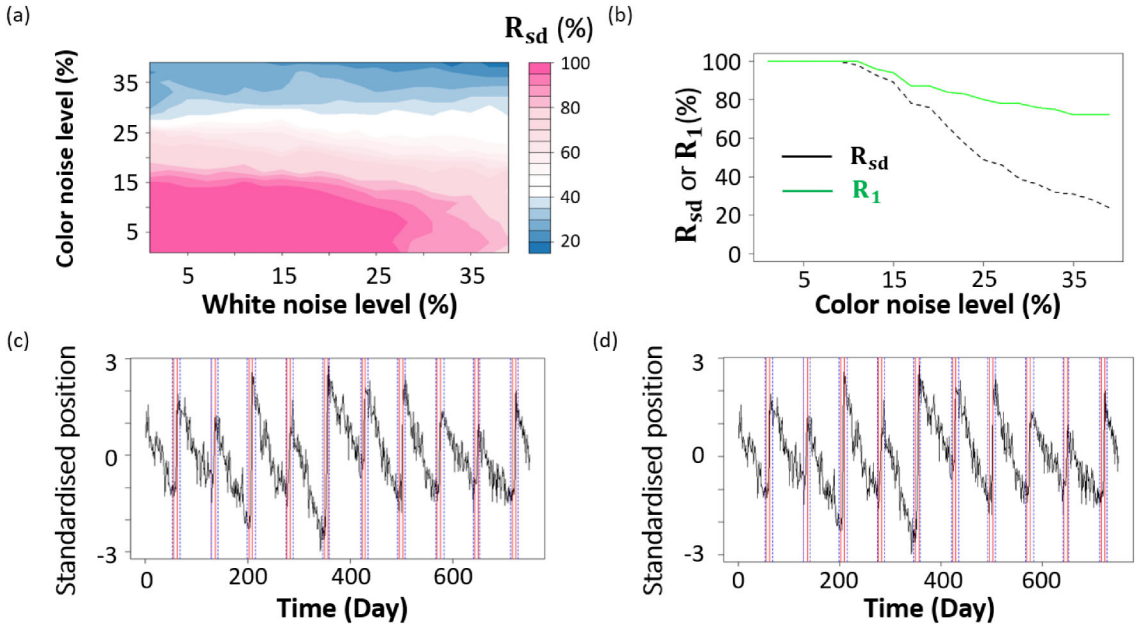

Figure 7. (a) The percentage of successful cumulative detection R_{sd} [see definitions in eq. (3)] for each simulated noisy data with different white and noise levels. For the same C_{wn} and C_{cn}, we generate 100 noisy data sequences using 100 seeds. (b) The percentage R_1 and R_{sd} as a function of colour noise level C_{cn} when the white noise level C_{wn} is fixed at 21 per cent. The locations of the change-points in two simulation examples with different noise levels are shown in (c) $C_{wn} = 21$ per cent and $C_{cn} = 11$ per cent; (d) $C_{wn} = 25$ per cent and $C_{cn} = 31$ per cent. Dotted vertical lines (blue): estimated change-points by SSAID; solid vertical lines (red): true change-points.

To provide a clear visual comparison of the performance of different methods, we now create a plot similar to an ROC curve as shown in Fig. 6(c). In this plot, a correct detection (an error of no more than 3 d from any true change-point) is defined as a true positive, while a false detection (an error of more than 3 d from any true change-point) is defined as a false positive. The (0,1) point (with 2×10^5 factored out) corresponds to the successful detection of all change-points. It is evident that the SSAID method is the closest to our expectation. Furthermore, since the definition of true and false positives depends on the pre-defined threshold of accepted error (3 d in our tests, indicated by the red circle with a cross), we varied this threshold from 1 to 20. The results consistently show that the detection of SSAID remains the closest to the (0,1) point, further verifying its good performance.

3.1.3 *Effect of colour noise*

We now investigate how colour noise influences the detection performance of SSAID. In GNSS time-series, noise typically comprises both white noise and colour noise, the latter being temporally correlated (M. Bos *et al.* 2013; K. Dmitrieva *et al.* 2015; M.S. Bos *et al.* 2020). This temporal correlation is often described using power-law models, where spectral amplitude changes according to $F(f) \propto f^{-n}$, with f representing frequency and n being the power-law index (D.C. Agnew 1992). In the realm of GNSS time-series, colour noise is often conceptualized as a combination of flicker noise ($n = 1$) and random walk ($n = 2$), or with a non-integer power-law index (J. Zhang *et al.* 1997; A. Mao *et al.* 1999). Most studies indicate that the optimal representation of time-dependent GNSS noise is flicker noise, with little or no random walk component (J. Zhang *et al.* 1997; S.D. Williams *et al.* 2004; A.R. Amiri-Simkooei *et al.* 2007; M. Hackl *et al.* 2011; K. Dmitrieva *et al.* 2015). Consequently, in our subsequent analyses, we consider colour noise to consist solely of flicker noise.

To simulate synthetic noisy SSE data incorporating both white and colour noise, we augment eq. (2) with an additional term, that is,

$$r_t = C_{wn} \times \epsilon_t + C_{cn} \times \epsilon_t^*, \tag{4}$$

where ϵ_t^* and C_{cn} represent the flicker noise model and its noise level, respectively. The synthetic test results in Section 3.1.1 revealed that the SSAID detection performance diminishes as the white noise level increases. Consequently, we confine the variation of noise levels to a lower range, spanning 1 per cent to 40 per cent with an increment of 2 per cent. We generate 100 data sequences for the same white noise and colour noise levels, utilizing different seeds for each. In total, we obtain $20 \times 20 \times 100$ noisy time-series. Fig. 7(a) shows the percentage of successful cumulative detection R_{sd} for simulated noisy time-series with different white and colour noise levels. Notably, when $C_{wn} \leq 25$ per cent and $C_{cn} \leq 15$ per cent, R_{sd} can reach a maximum of 100 per cent. This underscores SSAID's capability to maintain high performance even in the presence of colour noise. However, as C_{cn} approaches 30 per cent, R_{sd} decreases to 20 per cent, independently from the white noise level. In addition, R_{sd} decreases to approximately 80 per cent when $C_{wn} \geq 30$ per cent and $C_{cn} \leq 15$ per cent. This highlights the sensitivity of SSAID performance to noise levels, particularly to colour noise.

The Group 1 tests show that SSAID effectively detects SSEs under low noise levels, outperforming existing methods, though performance degrades with higher noise or stronger temporal correlation, a limitation shared by current approaches. The present investigation examines performance across a range of noise conditions, but these remain simplified compared to real GNSS data and do not capture the effects of SSE amplitudes or sign changes. To further assess robustness, we introduce two additional groups of synthetic tests in later sections, where more realistic noise is

Table 1. True positives and false positives in group 2 tests

Component	Method	True positives	False positives	Precision[y]
East	L1FT	9803	6790	0.5908
East	SSAID	8768	5480	0.6154
North	L1FT	9542	6679	0.5882
North	SSAID	8162	5489	0.5979

[y] $\text{Precision} = \frac{\text{True Positives}}{\text{True Positives} + \text{False Positives}}$

generated and SSEs are analytically modelled with controlled amplitudes. Further details about these additional tests are provided in Section S6 of the supplement.

3.2 Group 2 tests: analytical SSEs with irregular amplitudes and realistic noise conditions

We now conduct tests to evaluate SSAID's detection performance under more realistic conditions. The noisy time-series is generated in the same manner as in Group 1 (see eq. 1), but the underlying SSE signal is modelled using a logistic function defined by three parameters: amplitude, midpoint time and duration (G. Costantino *et al.* 2023; X. Xue & J.T. Freymueller 2023). Unlike Group 1, where the SSE signal is simulated using a deterministic fault slip model, this logistic-based approach provides greater flexibility in controlling the signal characteristics, particularly the SSE amplitude, which is a key factor influencing detection performance. In contrast, the deterministic model produces limited and lower amplitude slip histories due to simplified fault settings, which may not reflect signals detectable in real GNSS observations.

In Group 2, we simulate 10 SSEs in a two-year period (see Fig. S18 in the supplement), each with distinct amplitude jumps. The amplitudes (in mm) of the 10 simulated SSEs are: 1, 1.5, −2, 2.5, −3, 2, −2.5,−1.5, 1 and −1. Some events exhibit no change in sign. For instance, the first and tenth SSEs have equal amplitude magnitudes but opposite signs; similar pairings include the second and eighth, third and sixth and fourth and seventh SSEs. The noise component r_t is generated using the FAKENET software (D.C. Agnew 2013) and is composed of white noise, flicker noise and random walk noise:

$$r_t = C_{\text{wn}} \cdot \epsilon_t + C_{fk} \cdot \epsilon_t^* + C_{rw} \cdot \epsilon_t^+, \tag{5}$$

where ϵ_t^*, and ϵ_t^+ represent flicker noise, and random walk processes, respectively. C_{fk}, and C_{rw} are their corresponding noise amplitudes. The noise levels follow the estimates in J. Langbein & J.L. Svarc (2019), which are derived from analysis of ten years of GNSS time-series collected at 885 GPS stations. These stations are installed across the western United States, with coverage primarily focused on the Pacific Northwest, including Washington, Oregon and Northern California. In this simulation, we include all these 885 stations, each with two horizontal components (east and north), resulting in 1770 synthetic time-series with realistic noise levels. Fig. S19 in the supplement shows the distribution of noise levels for three noise types (white noise, flicker noise and random walk) in the east and north components. Across all three noise types, the distributions are generally similar between the east and north components, with the north component exhibiting slightly higher median noise levels. Specifically, the medians for white noise, flicker noise and random walk are 0.583, 0.541 and 0.353 for the east component, and 0.625, 0.552 and 0.371 for the north component (J. Langbein & J.L. Svarc 2019).

The detection results of both SSAID and l_1 linear trend filtering are shown in Figs S20–S23 in the supplement. To evaluate the detection accuracy of the two methods, we first define how true positives and false positives are determined. A detected change-point is considered a true positive if it falls within ±3 d of a known SSE's start or end time. For each known SSE, only one such detection is counted as a true positive; any additional detections within the window are treated as false positives, and other detections that do not correspond to any known SSE within the 3-d tolerance are also regarded as false positives. For each component (east or north), we simulated 885 time-series with different noise levels, all sharing the same underlying SSE signal containing 10 SSEs. Each SSE has two change-points corresponding to its start and end, so we expect to detect 17 700 true positives for each component without false positives.

Table 1 shows that SSAID produces 5480 false positives for the east component and 5489 for the north component. In contrast, l_1 trend filtering yields 6790 and 6679 false positives for the east and north components, respectively, indicating a lower false positive rate with SSAID. For true positives, l_1 trend filtering detects 9803 events for the east component and 9542 for the north component, while SSAID identifies 8768 and 8162, respectively. l_1 trend filtering consistently detected approximately 10 per cent more true positives than SSAID for both components. Although SSAID produces fewer true positives, it successfully detects all known SSEs. To quantify the detection performance of each method, we focus on the common metric of precision (see formula in Table 1), as our current evaluation does not allow a direct definition of false negatives. In this setup, detected change-points are classified only as true positives or false positives, meaning we only have false and true positives. For the east component, l_1 trend filtering achieves a precision of 59.08 per cent, while SSAID attains 61.54 per cent. For the north component, the precision is 58.82 per cent with l_1 trend filtering and 59.79 per cent with SSAID. These results indicate a slight improvement of approximately 1 per cent in precision for both components when using SSAID.

We now investigate the influence of SSE sign changes on detection performance. As noted earlier, we designed four pairs of SSEs with identical amplitudes but opposite signs. Using both SSAID and l_1 trend filtering, we assess the number of true positives detected for each SSE pair and for both the east and north components. From the first to the fifth SSE, the amplitude increases (in absolute value), followed by a drop at the sixth, another peak at the seventh and a gradual decline thereafter. The number of true positives detected across 885 GPS stations closely follows this trend (see Fig. 8a), indicating that detection performance is strongly influenced by the amplitude of the SSEs. In general, SSEs with larger amplitudes result in more true positives and are therefore easier to detect, regardless of the method used.

To assess the effect of sign change, we specifically compare the four SSE pairs with equal magnitude but opposite sign: the 1st and 10th SSEs (±1 mm), the 2nd and 8th (±1.5 mm), the 3rd and 6th (±2 mm) and the 4th and 7th (±2.5 mm). In each case, the

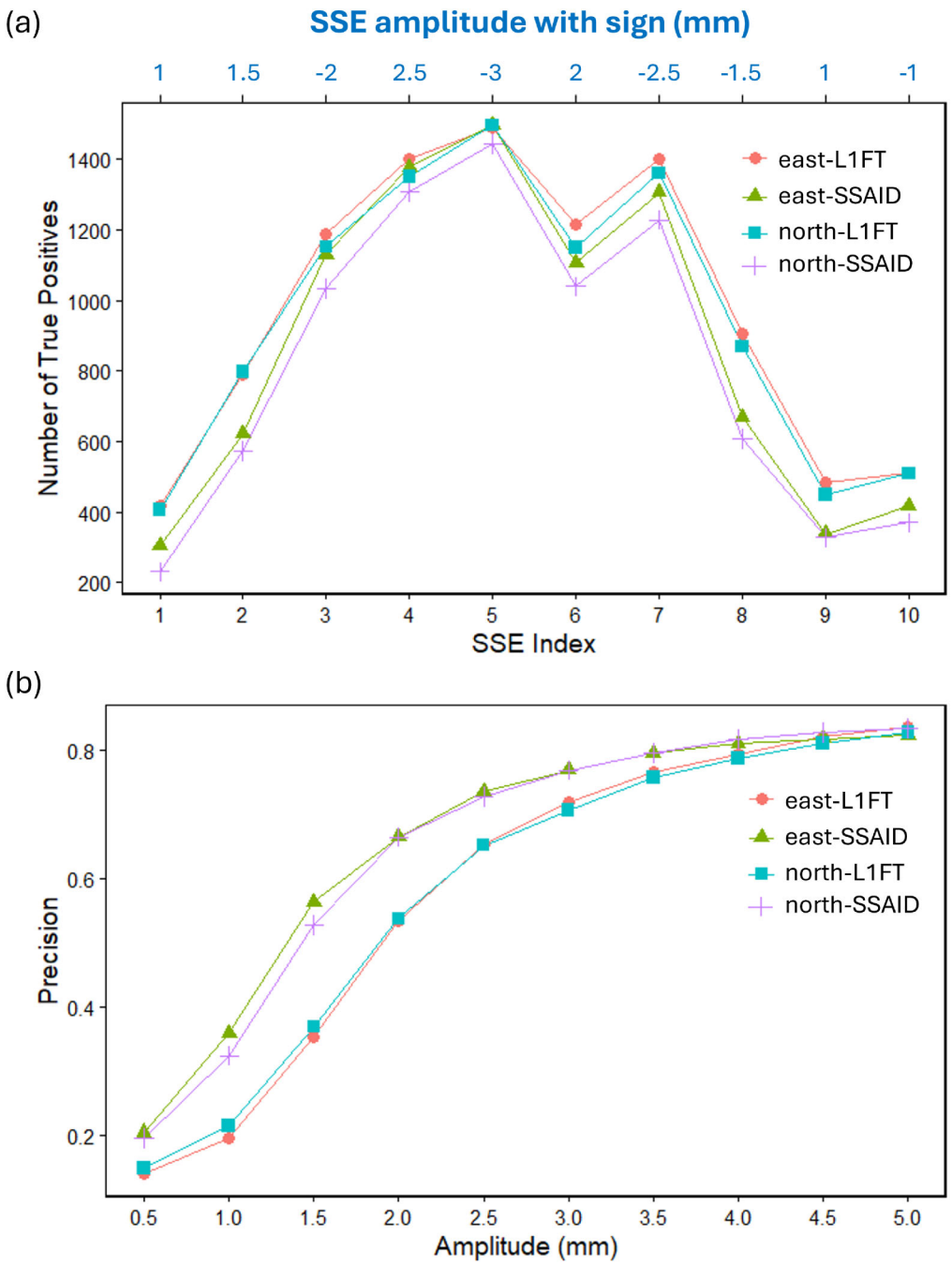

Figure 8. (a) Number of true positives detected by l_1 trend filtering and SSAID for the east and north components. The top of the panel displays the signed amplitude for each simulated SSE, using the same SSE indices shown below. (b) Comparison of detection precision by l_1 trend filtering and SSAID with different SSE amplitudes.

number of true positives is nearly identical between the positive and negative events. This confirms that the sign of the amplitude does not significantly affect the detection performance for either method.

Group 2 tests show that our method achieves comparable detection precision to the competing method while producing fewer false positives, and confirm that SSE amplitude affects detection performance, whereas sign change does not. However, the irregular amplitude variations used in these tests do not reflect the more regular patterns seen in real SSEs. In the final group of tests, we therefore investigate detection performance under more realistic, regularly recurring patterns with controlled amplitudes.

3.3 Group 3 tests: analytical SSEs with regular amplitudes under realistic noise conditions

We now repeat the Group 2 tests, but with SSEs following a more regular amplitude pattern without sign changes, while still including 10 SSEs in each time-series. Specifically, the amplitudes are varied from 0.5 to 5 mm in increments of 0.5 mm, resulting in 10 repeated tests of Group 2. In each repeat, the 10 SSEs share a uniform amplitude, and the data include both east and north components across 885 GPS stations. The noise levels are the same as those used in Group 2 (see eq. 5). These tests are designed to evaluate how the amplitude of regular SSEs influences detection performance.

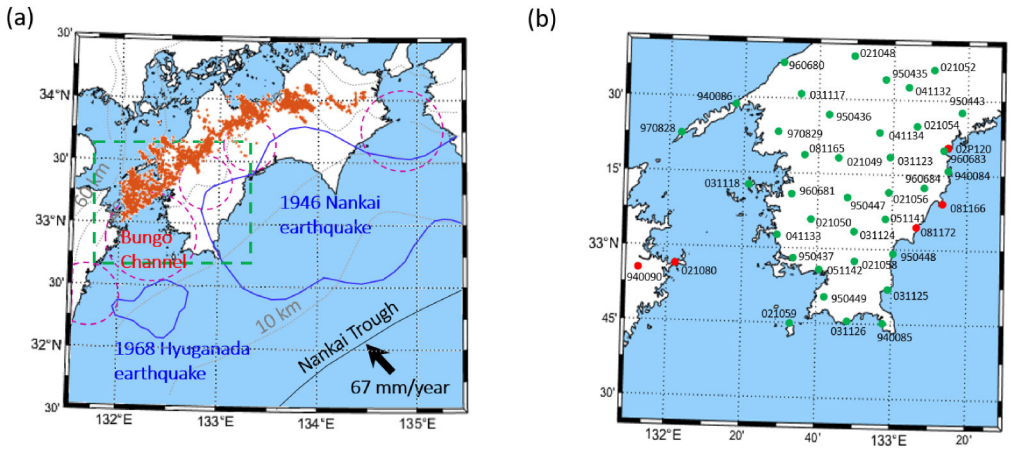

Figure 9. (a) The distribution map of earthquakes in the study area of southwest Japan, which is re-plotted based on H. Hirose & T. Kimura (2020). The magenta dashed circles and the blue contours denote the source areas of long-term SSEs (H. Hirose *et al.* 1999; A. Kobayashi 2010, 2012; H. Yarai & S. Ozawa 2013; R. Takagi *et al.* 2019) and megathrust earthquakes (Y. Yagi 1998; T. Sagiya & W. Thatcher 1999), respectively. The orange dots show the epicentres of tremors (K. Obara *et al.* 2010). Grey dashed lines indicate the depth of the subducting Philippine Sea plate (T. Baba *et al.* 2006; K. Shiomi *et al.* 2008). (b) The distribution map of 36 GNSS stations utilized in the current case study (see Section 5). This area is outlined by the dashed green box in panel (a). Both red and green circles indicate the location of GNSS stations, and the numbers near to circles refer to the GNSS station names. Note that we apply SSAID to detect change-points in SSE data recorded by GNSS stations identified as green filled circles in the case study reported in Section 5.

Fig. 8(b) shows that the precision of both SSAID and l_1 trend filtering increases with SSE amplitude in both components. Overall, SSAID consistently achieves higher precision than l_1 trend filtering, although the difference diminishes as amplitude increases and becomes negligible above 4.5 mm. Figs S24 and S25 in the supplement further demonstrate that SSAID produces substantially fewer false positives, particularly at lower amplitudes, while the advantage decreases as amplitude grows. In contrast, l_1 trend filtering consistently detects a higher number of true positives, however both methods successfully identify all simulated SSEs across the 885 GPS stations in both east and north components. Group 3 tests reveal that SSAID can achieve improvements of up to 20 per cent in precision [e.g. for SSE amplitudes of 1.5 mm, Fig. 8(b)] compared to l_1 trend filtering. This larger improvement, relative to the 1 per cent observed in Group 2 tests, is also attributable to SSA's strength in extracting periodic oscillations rather than irregular signals. Fig. 8(b) also shows that both l_1 trend filtering and SSAID consistently achieve slightly higher precision scores in the east component than in the north component for smaller SSE amplitudes ($\leq$ 2.0 mm). This observation is consistent with our analysis of noise levels across the 885 stations, which indicates that the north component generally exhibits higher noise across all noise types (see Fig. S19 in the supplement).

4 DATA AND PROCESSING

We use SSE data from the Nankai subduction zone which has a dense geodetic observation network. In southwestern Japan, the Amurian plate overriding the Philippine Sea plate converges to N50°W at a rate of about 67 mm yr^{-1} (S. Miyazaki & K. Heki 2001; T. Nishimura 2014; M. Kano & A. Kato 2020; K. Obara 2020). Both long-term and short-term SSEs occur across the Nankai Trough (K. Obara 2020) (see Fig. 9a). Short-term SSEs in southwest Japan generally exist in the deeper extension of long-term SSE regions.

Our SSE data are obtained from 36 GNSS stations of the GNSS Earth Observation Network System (GEONET) operated by the Geospatial Information Authority of Japan (GSI). These GNSS stations are distributed in the Shikoku region along the Bungo Channel (see Fig. 9b). The analysis period for this study is from 2008 January 1 to 2009 June 30. The vector $\mathbf{u}(t)$ of coordinates at each GNSS station, containing east, north and upward displacement, has been transformed to the 2005 International Terrestrial Reference Frame (ITRF2005), and can be generally modelled as a sum of different processes (R. Nikolaidis 2002; J.L. Davis *et al.* 2012; X. He *et al.* 2017; J. Bedford & M. Bevis 2018), that is

$$\mathbf{u}(t) = \mathbf{d_0} + \mathbf{m_0}t + \sum_{j=1}^{n_o} \mathbf{b_j} H(t - t_j) + \sum_{i=1}^{n_s} \mathbf{h_i}(t - t_i) + \boldsymbol{\xi}_{\mathbf{seas}}(t) + \boldsymbol{\xi}_{\boldsymbol{u}}(t) + \boldsymbol{\xi}_{\mathbf{SSE}}(t) + \boldsymbol{\epsilon}(t), \quad (6)$$

where t is the time, $\mathbf{d_0}$ and $\mathbf{m_0}$ refer to vectors describing the position of the reference site and the secular velocity, respectively. Here, we refer to the displacement rate of the linear process without the occurrence of other fault slips as the secular velocity, which represents the secular tectonic motions of two contacting plates of the subduction zone. The third term $\sum_{j=1}^{n_o} \mathbf{b_j} H(t - t_j)$ describes the vector of offsets due to non-tectonic changes such as antenna or other instrument changes, where n_0 is the number of non-tectonic changes, t_j is the time when the j-th non-tectonic change occurs and $H(t)$ is the Heaviside step function. The fourth term $\sum_{i=1}^{n_s} \mathbf{h_i}(t - t_i)$ represents the vector of coseismic and post-seismic movements from ambient regular earthquakes, where n_s is the number of ambient regular earthquakes, t_i is the time at which the i-th regular earthquake occurs and $\mathbf{h_i}$ refers to the coseismic and post-seismic movements from the i-th regular earthquake (S. Wdowinski *et al.* 1997; T. ElGharbawi & M. Tamura 2015). The other vectors $\boldsymbol{\xi}_{\mathbf{seas}}(t)$, $\boldsymbol{\xi}_{\boldsymbol{u}}(t)$, $\boldsymbol{\xi}_{\mathbf{SSE}}(t)$ and $\boldsymbol{\epsilon}(t)$ describe the movements from seasonal motions, unmodelled non-tectonic transients, SSEs and noise, respectively.

These SSE data have been pre-processed by T. Nishimura *et al.* (2013) to remove known effects from non-SSE processes. We now briefly illustrate the data processing procedures conducted on the raw GNSS data (T. Nishimura *et al.* 2013; T. Nishimura 2014; M. Fujita *et al.* 2019; T. Nishimura 2021). First, T. Nishimura *et al.* (2013) eliminated the coseismic offsets from six ambient large earthquakes (see the detailed catalogue therein), which are estimated by the difference in the 10-d averages of the daily coordinates before and

after the earthquakes. Secondly, the spatial filtering technique of S. Wdowinski *et al.* (1997) was applied to suppress the common mode errors for these stations, which are a major type of spatially correlated noise sources in GNSS data (D. Dong *et al.* 2006). Finally, the offsets from non-tectonic changes [i.e. the third term in eq. (6)] such as antenna maintenance were removed by the same method as that used to remove coseismic offsets. Note that the post-seismic deformations from nearby large earthquakes were not removed [i.e. the fourth term in eq. (6)], however their impacts are negligible in our current application as no obvious large earthquakes were identified in the period analysed (i.e. from 2008 January 1 to 2009 June 30) in the research area (T. Nishimura *et al.* 2013).

We denote the processed daily cumulative displacement vector at each station as

$$\bar{\mathbf{u}}(t) = \bar{\mathbf{b}}_0 t + \bar{\boldsymbol{\xi}}_{\mathbf{seas}}(t) + \bar{\boldsymbol{\xi}}_{\boldsymbol{u}}(t) + \bar{\boldsymbol{\xi}}_{\mathbf{SSE}}(t) + \bar{\boldsymbol{\epsilon}}(t), \tag{7}$$

where we use the same notation for each component as that in eq. (6), but place a bar above each quantity to indicate that these parameters represent cumulative displacements rather than daily displacements. The daily cumulative displacement $\bar{\mathbf{u}}(t)$ contains three components along different directions (i.e. east, north and upward), which are denoted as $\bar{u}_e$, $\bar{u}_n$, $\bar{u}_z$, respectively. In the following application, we concentrate on the N50°W component of the daily cumulative displacement at each station, denoted by X_t, which is parallel to the plate convergence direction of the Nankai Trough (see Fig. 9a). This is done by rotating two horizontal components (i.e. east and north) using the following equation,

$$X_t = \bar{u}_e \sin\bar{\delta}_0 - \bar{u}_n \cos\bar{\delta}_0, \tag{8}$$

where $\bar{\delta}_0$ is the azimuth angle of the plate convergence direction [see the black arrow in Fig. 9(a); $\bar{\delta}_0 \approx 50^\circ$ in Nankai Trough]. In the following applications, we further remove the daily secular motions and outliers from X_t at each station, through linear least squares and the four-sigma limit, respectively (J. Gazeaux *et al.* 2013; T. Nishimura 2021). Note that when conducting hypothesis tests in Section 5.2, we do not remove the daily secular motions, as they can be used to investigate the sign change of the displacement rate from the secular velocity when SSEs arise (K. Yano & M. Kano 2022).

5 APPLICATION TO OBSERVED DATA

We now apply SSAID to detect change-points in the real SSE data introduced in Section 4. Unlike synthetic tests, where SSE start and end times are explicitly defined and detection performance can be directly quantified, no direct criteria exist to validate detections from real GNSS data. We follow the same approach as K. Yano & M. Kano (2022) to validate SSAID detection results, which includes hypothesis testing, correlation with non-volcanic tremors and fault model estimation. This validation approach requires knowledge of both the start and end times of an SSE. However, SSAID may detect only a single change-point per SSE, so we introduce an additional step to post-process detected change-points, ensuring each SSE candidate has both a start and an end time before applying the validation procedures.

5.1 SSAID detection results and post-processing

We first present the raw results of detected change-points using our SSAID method in Fig. 10(a) (see green triangles). As previously discussed, each SSE candidate should be represented by both a starting and an ending change-point, therefore, the number of detected change-points at each of the 36 stations is expected to be even. However, Fig. 10(a) shows that only 13 of these satisfy this condition (see station names highlighted in red). This implies that SSAID in most stations misses some change-points associated with SSEs and/or detects spurious change-points not associated with SSEs. We also observe in multiple stations that the time difference between two neighbouring detected change-points can be in the order of months [e.g. the first and the second change-points in Fig. 11(a), which shows the GNSS data recorded at station 970828]. Such a long duration is not consistent with past studies in this region, which show that potential short-term SSEs during the period analysed last about 7 d (H. Hirose & K. Obara 2010; K. Obara & A. Kato 2016; K. Obara 2020). Therefore, two neighbouring change-points with a large time difference cannot be paired as the start and end times of the same SSE. The above observations indicate that many single change-points, corresponding to either the start or end of an SSE, were identified as potential SSEs [e.g. see green lines in Fig. 11(a)]. In the synthetic simulations (see Fig. 1), each SSE is shown with two change-points: a vertical red line for the start and a vertical dotted blue line for the end. In the current application, however, many detected change-points represent only one of the two required points for an SSE. This suggests that the second change-point needed to complete the pair was often not detected. Additionally, as noted earlier, applying the approach of K. Yano & M. Kano (2022) to validate detected change points as true SSEs requires both the start and end of an SSE, that is, a pair of change-points.

To remedy this pathology, we introduce an additional procedure, preceding the validation steps, to process the raw detected change-points such that each SSE candidate is represented by a pair of change-points corresponding to its start and end times. This is done by creating artificial change-points to pair with the detected single change-points. The procedure consists of the five following sequential steps (see Section S10–S11 and Figs S26–S28 in the supplement for additional details):

(i) **Initial fit**: A piecewise-linear model is fitted to the noisy SSE data using change-points identified by SSAID [e.g. the orange line in Fig. 11(a) and the change-points in Fig. 10(a)]. This initial fit establishes the baseline structure for all subsequent analyses.

(ii) **Slope calculation**: The slope of each segment is computed to quantify local trends and provide the basis for classifying change-points.

(iii) **Identification of single and paired change-points**: Change-points are identified as either single or paired. For single change-points, we also determine whether they correspond to the start- or end-time of an SSE. This classification guides the targeted pairing of single change-points.

(iv) **Generation of artificial change-point candidate pairs**: For each identified single change-point, an array of potential companion change-point is created in a window spanning 3–7 d before and after the detected single change-point. This interval is chosen to match the average duration of short-term SSEs reported in previous studies (see detailed procedure below). Each combination of an original single change-point and a candidate companion change-point in that time window is referred to as a 'change-point candidate pair'.

(v) **Evaluation and selection of the best candidate**: Each candidate pair is evaluated by refitting a piecewise-linear model that incorporates both the original and candidate change-points. The model fitting performance is quantified using the strengthened Schwarz Information Criterion (sSIC) (J. Liu *et al.* 1997; P. Fryzlewicz 2014), which balances goodness-of-fit against model complexity. For each

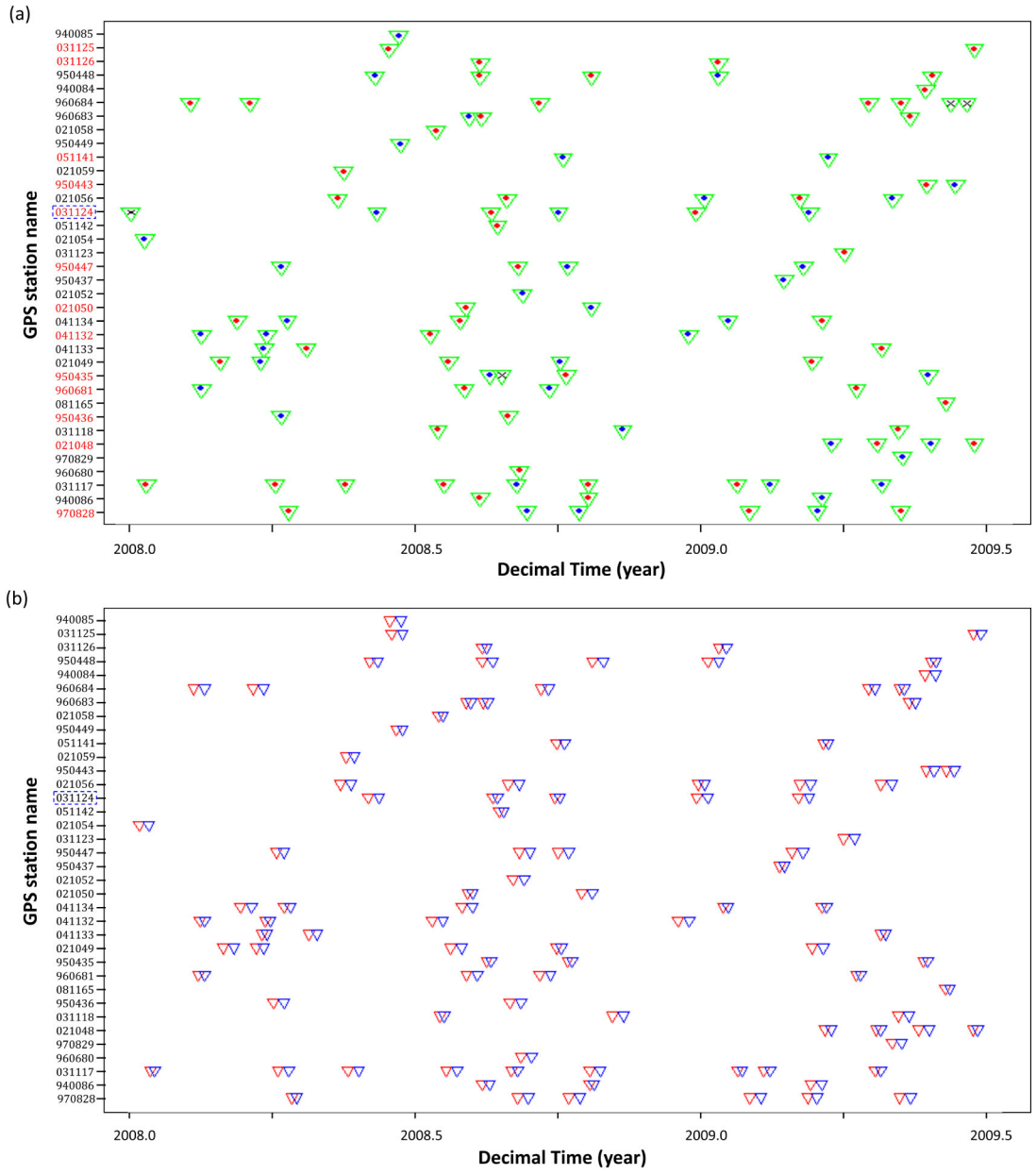

Figure 10. (a) Detected change-points by SSAID in GNSS data recorded by the 36 GNSS stations, shown in Fig. 9(b). Station names for which the number of detected change-points is even are highlighted in red. Red dots, blue dots and black crosses inside the green triangles indicate the identified starting, ending and discarded change-points in panel (b), respectively. (b) Post-processed results of detected change-points shown in panel (a). Each pair of adjacent triangles in panel (b) represents the starting and ending change-points of a detected SSE candidate, with the first triangle (red) marking the start and the second (blue) marking the end. *The figure, and subsequent similar figures, are plotted by sorting the stations along the direction of N50°W, which is perpendicular to the Nankai Trough*.

single change-point, the candidate pair with the lowest sSIC is selected, ensuring that only those pairs that meaningfully improve the model without overfitting are retained (Y.C. Yao 1988; J. Liu *et al.* 1997; P. Fryzlewicz 2014).

We now illustrate how to pair detected change-points based on the calculated slopes of the segments between change-points and identified single change-points (i.e. the Step 3). We refer to k_b^i and k_a^i as the slope of the segment before and after the i-th detected change-point, respectively. We pair two consecutive change-points (i-th and $(i+1)$-th, say) as the start and end times of a unique SSE, if they simultaneously satisfy the following conditions: (1) k_b^i has the same sign as the secular displacement rate; (2) the sign of k_a^i is opposite to that of the secular displacement rate; (3) the time difference between the two neighbouring change-points (i.e. the duration of the SSE) is no more than a duration threshold, denoted by $D_{\max}$. Here, we estimate the sign of the secular displacement rate (i.e positive or negative) at each GNSS station by taking the slope of a linear model fitted to the whole noisy data. All change-points that have not been paired are then classified as single change-points. In the study area considered, the expected duration of an SSE is $3-7$ d (K. Obara 2020).

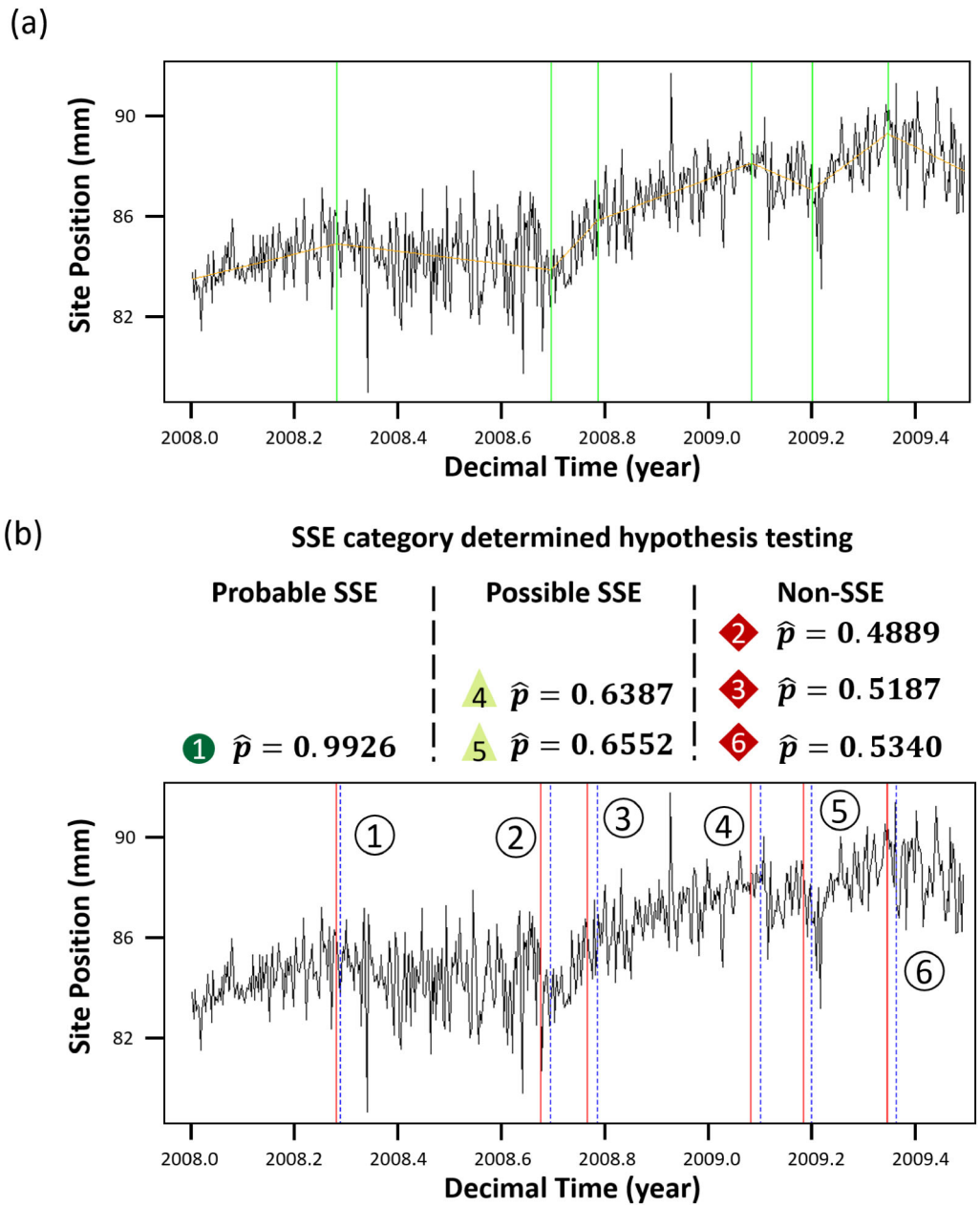

Figure 11. (a) Observed GNSS data recorded by station 970828 (see the black line) and the fitted piecewise-linear signal (see the orange line) using detected change-points by SSAID (see solid vertical lines in green); (b) New paired change-points of the same station 970828 based on detected change-points in panel (a). Solid vertical lines (red): starting change-points; dotted vertical lines (blue): ending change-points. The calculated probabilities of SSE occurrences $\hat{p}$ for each pair of change-points are included on the top of panel (b) and their associated SSE categories. The markers used for different SSE categories are the same as those in Fig. 12, and the numbers inside markers are consistent with the numbers in circles in panel (b), that is, the indexes of change-point pairs.

We found that the detected change-point location error by SSAID is at most 3 d (see Section S3 and Fig. S8(b) in the supplement). In the worst case, an SSE with duration 7 d could be detected by a pair of change-points separated by up to 14 d (assuming maximum error). Therefore, we set $D_{\max}$ as 14 d. Fig. 10 shows that the majority of raw detected change-points are classified as single change-points.

We then generate candidates of artificial change-points to pair with each single change-point (i.e. the Step 4). We first assume that each single change-point is associated with either the start or the end time of an SSE, and the duration of SSEs is $3-7$ d. This implies that the undetected change-point candidates are located in a window spanning $\pm(3-7)$ d around the detected single change-point. To be more specific, if the detected single change-point is the start time of an SSE, denoted by $\bar{x}_{\text{cp}}$, the associated change-point candidates for the undetected end time of this SSE include $\bar{x}_{\text{cp}}+3$, $\bar{x}_{\text{cp}}+4$, $\cdots$, $\bar{x}_{\text{cp}}+7$; conversely, if it is the end time of an SSE, the candidates for the start time are $\bar{x}_{\text{cp}}-7$, $\bar{x}_{\text{cp}}-6$, $\cdots$, $\bar{x}_{\text{cp}}-3$. Based on the slopes of two consecutive segments fitted in Step 2, we can determine if each single change-point is the start or the end time of an SSE. We have three possible situations: (1) if k_b^i and k_a^i have the same and the opposite sign as the secular displacement rate, respectively, then we regard the detected single change-point as the start time of an SSE; (2) if k_b^i and k_a^i have the opposite and the same sign as the secular displacement rate, respectively, then we regard the detected single change-point as the end time of an

SSE; (3) in other cases, the detected single change-point can be the start time or the end time of an SSE.

Next, we fit different piecewise-linear curves through the GNSS data for every change-point candidate pair (i.e. the Step 5). The number of fitted piecewise-linear curves for each single change-point corresponds to the number of change-point pair candidates. If the single change-point is either the starting or ending point, there will be five change-point candidate pairs, resulting in five piecewise-linear curves. However, if the type of the single change-point is unknown, there will be 10 change-point candidate pairs, resulting in 10 piecewise-linear curves. We select the piecewise-linear curve best fitted to the noisy data through the sSIC. We then take the associated change-point candidate to pair with the single change-point, and obtain new paired change-points as shown in Figs 10(b) and 11(b), in which we have two change-points for the start and end times of each potential SSE (red and blue, respectively). In our analysis, SSAID detected a total of 105 change-points across the 36 stations during the analysed period, with nearly all raw detections identified as single change-points (see Fig. 10 a). Specifically, SSAID identified 57 starting change-points and 44 ending change-points. More than half of the detections failed to capture the end times of potential SSE candidates, suggesting that the onset of SSEs is easier to detect than their conclusion. Note that we also imposed some manual constraints on the paired change-points to avoid the overlaps of two neighbouring pairs and discard some single change-points with obvious deviations. For example, the first detected change-point in the station 031124 was identified as an ending change-point at the second day of the analysed period, while we expected the starting change-point to be $3-7$ d preceding the detected ending change-point, so that we discarded this change-point. We discarded four detected change-points in total (see Fig. 10a).

Note that this additional post-processing itself is not intended to accurately identify the true change-points of actual SSEs, nor to determine whether they originate from true SSEs. Its sole purpose is to generate a pair of change-point for each SSE candidate, enabling the application of the subsequent hypothesis testing and fault estimation for validation. Given the presence of complex noise and unmodelled non-tectonic movements, spurious detections in the raw change-points are expected, meaning that certain detected single change-points are not associated with actual SSEs. Even in such cases, the additional processing step will still create a paired change-point for these false single detections; however, these false pairs are subsequently rejected during hypothesis testing, the validity of which has been demonstrated through synthetic tests (see Section S11 in the Supplement).

5.2 Validation via hypothesis testing

We now implement the hypothesis testing approach proposed by K. Yano & M. Kano (2022) to quantify the probability that each SSE candidate corresponds to an actual SSE following the post-processing procedure described above. Here, the null hypothesis assumes that no SSE occurs, while the alternative hypothesis assumes that an SSE does occur. Unlike traditional hypothesis tests that calculate a p-value to assess the probability of rejecting the null hypothesis, the approach of K. Yano & M. Kano (2022) incorporates information from neighbouring stations to define a new metric, $\hat{p}_j^k$, which directly quantifies the confidence in the occurrence of an actual SSE. Here, $\hat{p}_j^k$ represents this metric for the k-th SSE candidate at the j-th station. A value of $\hat{p}_j^k$ closer to 1 indicates a higher probability that an SSE occurs.

This hypothesis test is based on the sign change of the displacement rate at the start time of an SSE. As discussed in Section 2, the overall trend of GNSS data is a noisy linear process if no SSE occurs, while the occurrence of an SSE redirects the original trend in a different direction. Upon completion of the SSE, the trend reverses back to its previous state. As shown in Fig. 1, the sign of the displacement rate at the start time of an SSE is opposite to that of the secular displacement rate. Note that the sign of the GNSS time-series displacement trend may remain unchanged when the seismogenic zone, nearing rupture in a large earthquake, slips faster than the transition zone, a short phase difficult to capture at the current daily resolution. As no large earthquakes occurred during our analysis period, we exclude this case and focus on general scenarios with a sign change, consistent with K. Yano & M. Kano (2022). Additional details of the hypothesis test can be found in K. Yano & M. Kano (2022) and Section S7 in the supplement.

5.2.1 *Classification of SSE candidates*

Fig. 12 presents the estimated probability of each detected change-point for the occurrence of an SSE by the null hypothesis test and its associated SSE category. We observe that at most stations SSAID can successfully detect SSEs with high confidence. At several stations, no such change-points are found, such as stations 021052 and 950449. The best detection happened at station 950447, in which all the four detected change-points have high confidence value of $\tilde{p}_j^k \geq 0.9$.

Based on the estimated $\tilde{p}_j^k$ values, we categorize the detected change-points into probable, possible and non-SSE candidates, if $\tilde{p}_j^k \geq 0.9$ and $\hat{N}_a^j > 1$; $0.6 \leq \tilde{p}_j^k < 0.9$ or $\tilde{p}_j^k \geq 0.9$ with $\hat{N}_a^j = 1$; and $\tilde{p}_j^k < 0.6$, respectively. These values were selected to be somewhat conservative in our attempt to confidently claim SSE detection. $\hat{N}_a^j$ refers to the number of stations neighbouring the j-th station (see more details about its definition in Section S7 in the supplement). The introduction of $\hat{N}_a^j > 1$ in the definition of probable SSE candidates is to guarantee that the detected change-points have a high confidence for the occurrence of SSEs at neighbouring stations within 30 km simultaneously, rather than at a single station (K. Yano & M. Kano 2022). Under the current classification rules, we only have a high confidence that detected change-points in the first group are associated with SSEs, and we are less confident that the other detected change-points are associated with SSEs. Fig. 12(b) indicates that we have identified 39 probable SSE candidates (see green circles) and 31 possible SSE candidates (see light green triangles) in total across all the stations. Note that some detected SSEs at different stations might be from the same SSE, indicating that the actual number of detected SSEs is likely less than the number stated above. In addition, detected change-points classified as non-SSEs still might be associated with SSEs, as other unmodelled non-tectonic movements or noise could affect the displacement field at the observation site so that the sign change does not significantly differ from the secular displacement rate (T. Nishimura *et al.* 2013). In the remainder of this study, we do not discuss these 2 groups further and instead we focus on the detected change-points in the first group of probable SSE candidates.

5.2.2 *Comparison and validation*

During the period analysed in our current study, four SSEs were identified in the western Shikoku region along the Bungo Channel by T. Nishimura *et al.* (2013) (see orange shaded-areas in Fig. 13(a);

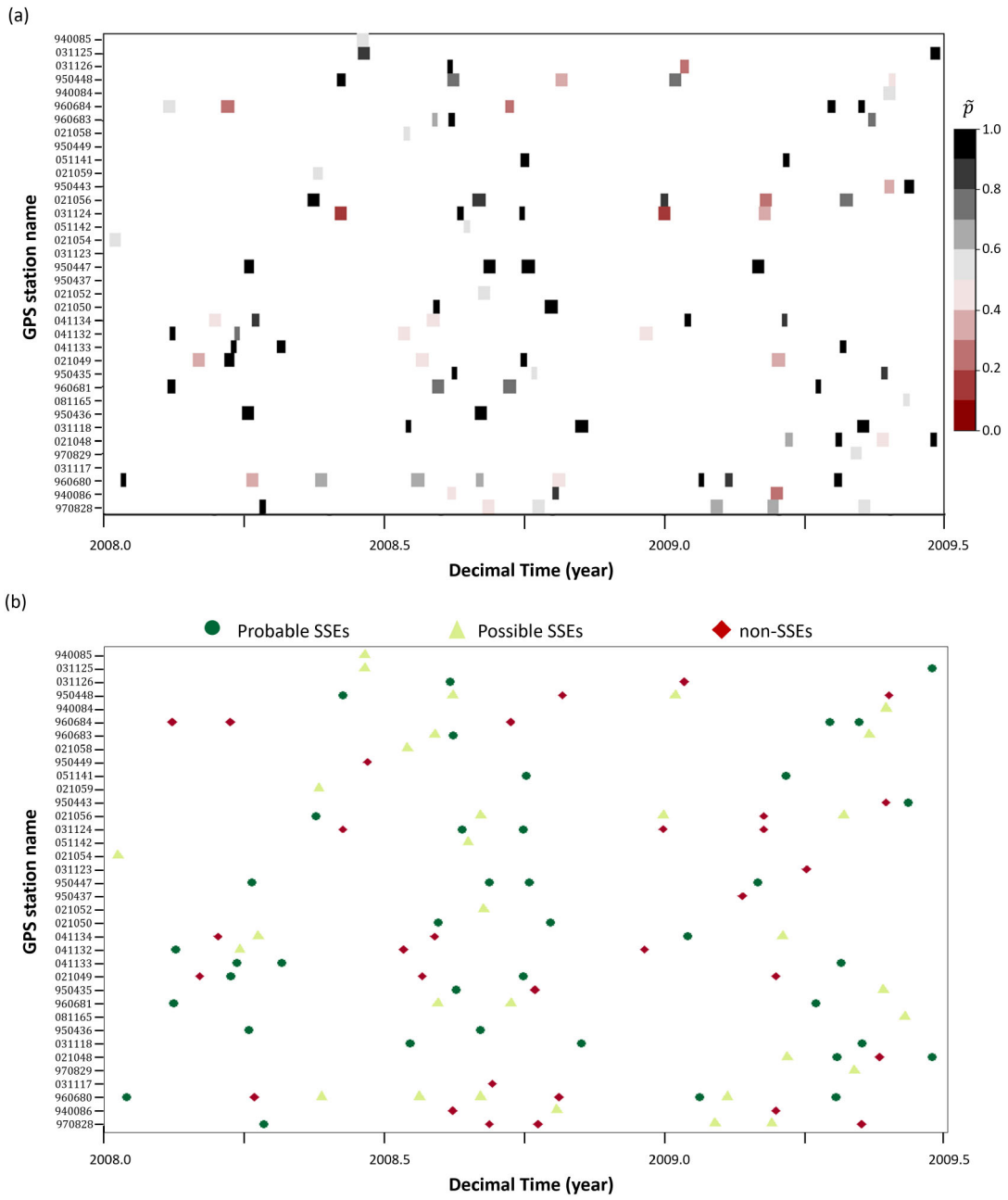

Figure 12. (a) Estimated confidence $\tilde{p}$ of each change-point pair shown in Fig. 10(b). The left and the right side of each rectangle refer to the starting and the ending change-point, respectively. (b) Detected SSEs categorized as probable SSEs (green circles), possible SSEs (light green triangles) and non-SSEs (red diamonds). The location of each marker refers to the middle time of each SSE candidate.

the associated SSE catalogue obtained from M. Kano *et al.*, 2018). Not only has our new method successfully detected all these four SSEs in various stations identified by T. Nishimura *et al.* (2013), but SSAID is also able to detect many more previously undetected probable SSE candidates. Note that it is not expected that all the SSEs can be recorded at each GNSS station, since the SNR and ground displacements caused by SSEs might greatly vary at different stations. If the SNR is too low or the ground displacement is too small at a certain station, the change-points associated with SSEs cannot be detected.

To further verify the validity of the newly detected probable SSEs, we investigate their correlations with the tremor occurrence, since tremors often accompany SSEs (G. Rogers & H. Dragert 2003; K. Obara & A. Kato 2016; T. Wang *et al.* 2018). An increasing daily number of tremors generally indicates that an SSE is probably occurring (Y. Ito *et al.* 2007). Note that the occurrence of SSEs is not always consistent with tremor activity, which means that SSEs can also occur when no tremor activity is detected (T. Wang *et al.* 2018; M. Kano & A. Kato 2020; K. Yano & M. Kano 2022). In addition, not all the observed tremors are associated with the occurrence of SSEs. Based on their recurrence pattern, the tremors in the Shikoku region have been categorized into three states: episodic; weak concentration and background by T. Wang *et al.* (2018), among which only the tremors in the episodic state occur during SSEs. Therefore, we count the number of daily tremors in the episodic state to investigate its correlation with SSEs. As the 36 GNSS stations used in our

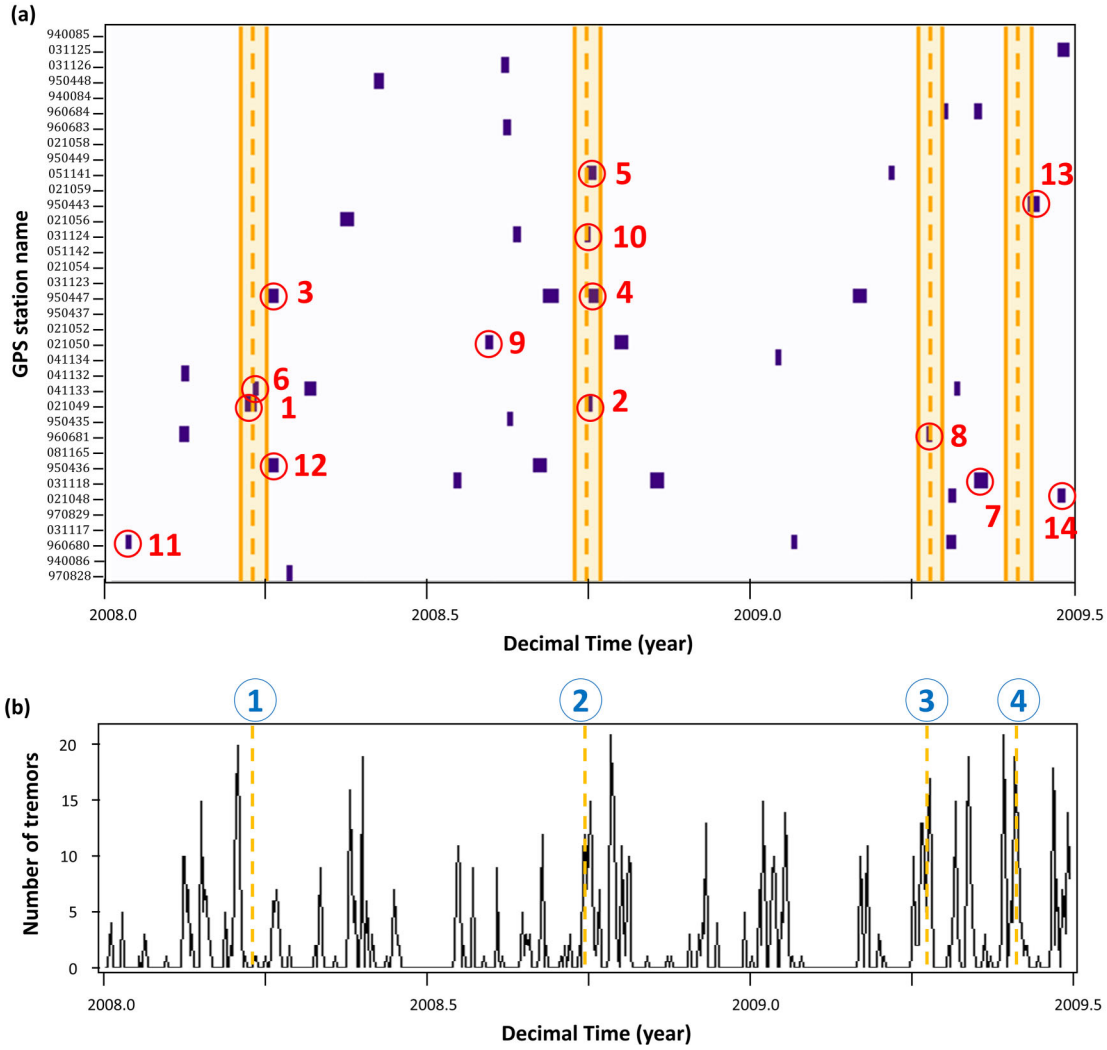

Figure 13. (a) The distribution of detected probable SSEs by SSAID, which are indicated by purple boxes. The left and the right sides of each purple box refer to the start and end times of an identified probable SSE by null hypothesis tests, respectively. Orange dotted lines in the middle of each shaded area refer to the occurrence times of SSEs identified by T. Nishimura *et al.* (2013). We assume that the start and end times of their identified SSEs are 7 d before and after the occurrence times, respectively. Purple boxes highlighted by red circles refer to probable SSEs identified by the fault estimation (see Section 5.3). The indices of these SSEs are shown as red numbers next to each circle, consistent with the inverted fault model presented in Fig. 14 and Figs. S38–S47 in the supplement. (b) The daily number of tremors in the episodic state. Numbers in circles on the top refer to the index of identified SSEs by T. Nishimura *et al.* (2013) in Shikoku region.

study are concentrated in the western Shikoku region (see Fig. 9b), we only utilize the episodic tremors around these GNSS stations (i.e. with state index 1–7 and 9–13 as indicated in T. Wang *et al.*, 2018), rather than the whole observed tremor catalogue in the Shikoku region. Figs 13(a) and (b) show that the identified probable SSEs are well concordant with tremor activity in the episodic states. We also note that at its highest peaks, the number of tremors is about 20, during the study period. By contrast, the total number of detected probable SSEs across the 36 GNSS stations during the same period, as determined by hypothesis testing, is 39. The number of SSEs suggested by the tremors is much lower than the identified probable SSEs. This discrepancy is reasonable because the SSE detection via hypothesis testing is on a per-station basis. In practice, the same SSE might be recorded simultaneously by different GNSS stations. Therefore, SSE detection in GNSS stations after hypothesis testing should be further validated by assessing spatial coherency across the regional network, as is done in the next subsection.

5.3 Fault estimation

Potential SSEs are expected to bring up a systematic pattern change in the displacement field at various stations, however the above hypothesis tests fail to consider such changes in the displacement field (T. Nishimura *et al.* 2013). This can be done by estimating a fault model to describe the observed displacements (T. Nishimura *et al.* 2013; T. Nishimura 2021; K. Yano & M. Kano 2022). We use a Bayesian inversion method, that is, the Markov chain Monte Carlo (MCMC) method with the Metropolis-Hastings algorithm (G. Olivares & N. Teferle 2013; M. Bagnardi & A. Hooper 2018; G. Olivares-Pulido *et al.* 2020; K. Yano & M. Kano 2022), to estimate a finite rectangular fault model with uniform slip for each detected probable SSE, and systematically investigate its associated displacement field. This rectangular fault model is the same as that used in Y. Okada (1985). Based on the processed cumulative displacement field as shown in eq. (7), we follow the approach of T. Nishimura

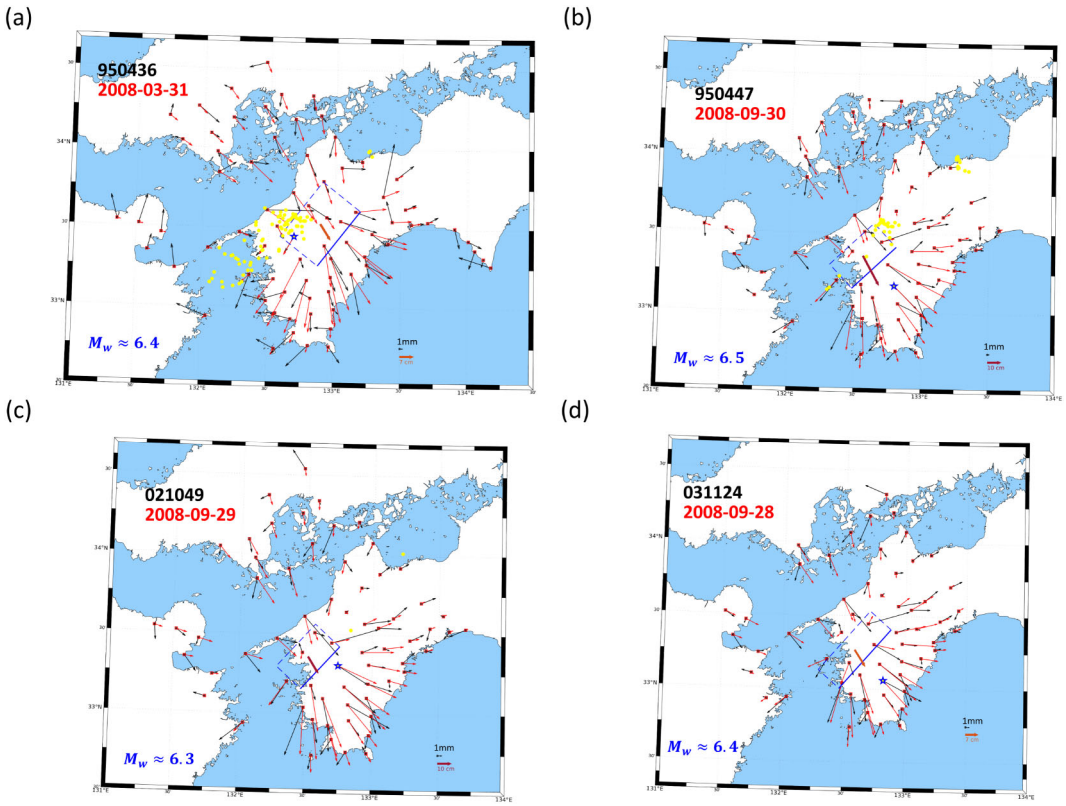

Figure 14. Representative examples of the estimated fault model for identified probable SSE candidates at the different stations: (a) station 950436; (b) station 950447; (c) station 021049; (d) station 031124. The date in red under the site name refers to the start date of this probable SSE candidate. The quantities M_w in blue colour refer to the estimated moment magnitude for these identified SSEs. The star in the map indicates the location of the station where this SSE candidate was identified. The black and the bold arrows in the right-bottom corner are the scale arrows for the observed displacement and the slip amount of the estimated model, respectively. The synthetic displacements (red arrows) generated by the displacement model of Y. Okada (1985) have the same arrow scale as the observed ones (black arrows). Yellow dots indicate the epicentre of tremors in the episodic state 5 d before and after the date (see the date on the left-upper corner) when this candidate was found. The blue solid line of the rectangle refers to the top edge of the estimated fault model. Note that the GNSS stations displayed in each panel correspond to those whose time-series are utilized for fault estimation. The specific stations included may vary depending on the location of the detected change-points and their neighbouring stations. Details of the inverted fault model parameters are provided in Table S3 of the supplement, along with the SSE index for each panel: (a) 12, (b) 4, (c) 2 and (d) 10. These SSE indices are consistent with those used in Fig. 13 (a).

et al. (2013) to calculate the displacement field for each SSE candidate at various GNSS stations. A linear model is fitted over a 180-d sliding window to estimate daily displacements, reducing the effect of noise, and these daily displacements are then summed over the duration of each SSE candidate to construct the displacement field. These estimated daily displacement variations are used to obtain the estimation of the fault parameters. A detailed exposition of the MCMC inversion method and its theoretical framework can be found M. Bagnardi & A. Hooper (2018) and K. Yano & M. Kano (2022).

For each identified probable SSE (see purple boxes in Fig. 13a), we only use the observed displacement data of neighbouring stations located within a designated range as the input data of the inversion. Here, the ranges that we utilize along the dip and the strike directions are 100 and 150 km, respectively, from the station where the probable SSE was identified (R. Takagi *et al.* 2019). We further rule out the data with a high percentage of invalid values (i.e. $\geq$ 20 per cent) during the period analysed in our study (T. Nishimura 2021). Note that although our detection focused on 36 stations within the research area, when performing the inversion to verify detection validity, we also utilized stations within the designated range but beyond the original 36 stations.

Our inversion follows the approach of K. Yano & M. Kano (2022) to fully explore the source parameters while we further assume that no tensile component occurs, thus nine source parameters (length, width, depth, latitude, longitude, strike, rake, slip and dip angle) need to be determined. The initial guesses for those nine source parameters are set as follows: the latitude and the longitude of the estimated fault are set as those of the station where the probable SSE candidate was identified; the length and the width are 50 and 35 km, respectively; the slip amount and the rake angle are 10 mm and 110°, respectively; the initial values for the strike, the dip and the depth are obtained by projecting the estimated fault model to the surface of the Philippine Sea Plate. To mitigate the effect of the initial model on the final inversion results, we further simulate nine realizations of the initial fault model obtained by randomly perturbing the default model described above. In total, we run the MCMC inversion 10 times for each detected probable SSE. We then choose the output of these 10 sets with the smallest residual as a new set of initial model parameters, and conduct a new inversion (M. Bagnardi & A. Hooper 2018; T. Nishimura 2021).

We estimate a final finite fault model for each probable SSE candidate. As the slip direction of the expected SSEs in the Shikoku region should be opposite to the plate convergence direction (i.e.

N50°W), we rule out probable SSEs candidates, for which slip directions are not between N100°E and N170°E (T. Nishimura *et al.* 2013). SSE candidates excluded based on this criterion may still represent actual SSEs, as inversion results are influenced by many factors (M. Bagnardi & A. Hooper 2018; K. Yano & M. Kano 2022). Short-term SSEs often produce subtle ground motions that can be masked by noise or recorded at only a few stations, preventing a coherent network-wide signal. Thus, while this fault estimation procedure provides a quantitative basis for classification, some rejected candidates may be true SSEs, and some accepted ones may still contain non-tectonic signals (T. Nishimura *et al.* 2013).

We obtain 14 potential SSEs in our current research area (see red circles in Fig. 13a). Fig. 14 shows representative examples of estimated fault models for four identified probable SSEs (see the other results in the supplement). These identified SSEs have an opposite slip direction to that of the plate convergence. The locations of some estimated faults coincide well with the epicentres of the tremors (see Figs 14a and b), suggesting the possible occurrence of episodic tremor and slip (ETS). We also note that no tremor activities were observed around the estimated fault model in Figs 14(c) and (d), even though the estimated location is still close to the locations of known SSEs (see Fig. 9a). We further estimate the moment magnitude (M_w) for all identified SSEs using the estimated fault models. M_w is calculated using the formula $M_w = \frac{2}{3}(\log M_0 - 9.1)$, where $M_0 = G \times D \times S$. In this formula, G represents the rigidity of the medium, D the rupture surface area and S the slip of the estimated fault model (P. Bormann & D. Di Giacomo 2011). We assume G to be 30 GPa. The estimated moment magnitudes of these identified SSEs range from 5.8 to 6.5, with most being between 6.0 and 6.4. This is consistent with the range of the magnitudes identified in past studies (T. Nishimura *et al.* 2013).

6 CONCLUSIONS

We developed a novel statistical method, labelled SSAID, to automatically detect short-term SSEs in GNSS data. We demonstrated its effectiveness on a range of noisy simulated SSE data and illustrated its superior detection performance compared to two existing detection methods, i.e. linear regression with ΔAIC and l_1 trend filtering. We then applied SSAID to detect short-term SSEs in observed GNSS data in the western Shikoku region. The results show that SSAID successfully detects multiple change-points in various GNSS stations. We utilized the null hypothesis test to identify probable SSE candidates from these detected change-points, based on the sign of the displacement rate being different from that of the secular displacement rate. These SSE candidates include all known SSEs identified by T. Nishimura *et al.* (2013) during the period analyzed, as well as previously undetected SSEs. We further estimated the parameters of a finite fault model generating the observed displacement field for each probable SSE candidate using a Bayesian inversion technique. Selecting the SSEs for which the azimuth directions of the slip vectors of the estimated fault models are opposite to that of the plate convergence, we managed to identify new SSEs in the western Shikoku region that should be added to the existing catalogue. Our results demonstrate the effectiveness of SSAID in detecting SSEs in observed GNSS data. Existing methods for detecting short-term SSEs require specifying a suitable threshold to identify the start and end change-points of SSEs. An inappropriate threshold can lead to the misestimation of the number of change-points, making detection performance heavily dependent on the threshold choice. Since different time series require different thresholds, selecting a suitable one for a group of time series is impractical. Our method, however, does not require specifying such parameters, offering greater general applicability to various time series. By relying only on a simple piecewise non-linear assumption, our method holds promise for detecting SSEs in other subduction zones using GNSS data such as the Cascadia subduction area, which we identify as an important direction for future validation.

ACKNOWLEDGMENTS

We are grateful to Professor Ting Wang (University of Otago) for her constant support, insightful discussions and technical assistance throughout this project. Her expertise and guidance played a crucial role in shaping the direction of this research. We would also like to thank Assistant Professor Akiko Takeo (University of Tokyo) and Professor Takuya Nishimura (Kyoto University) for kindly sharing the processed GNSS data and the geometry file of the Philippine Sea Plate surface with us. We further acknowledge the helpful comments and suggestions from Professor Takuya Nishimura on this work. We would also like to thank the review team for their valuable help in improving the manuscript, including the lead editor Professor Duncan Agnew, the second editor Professor Carl Tape, the reviewer Associate Professor Masayuki Kano, the two anonymous reviewers and the assistant editor Louise Alexander for their thoughtful comments and support. We also acknowledge the use of the eResearch Infrastructure Platform, hosted by the Crown company Research and Education Advanced Network New Zealand (REANNZ) Ltd, for supporting the simulations in this work. YM was supported by a University of Otago Doctoral Scholarship, and University of Otago Postgraduate Publishing Bursaries (Doctoral).

DATA AVAILABILITY

The simulated SSE data used for numerical tests in the study and the code of the newly developed method SSAID are available at Zenodo (Y.M. Ma,2025), which are provided for private study and research purposes and are protected by copyright with all rights reserved unless otherwise indicated. The observed GNSS data utilized in this study can be requested through Geospatial Information Authority of Japan (GSI) at https://www.gsi.go.jp/ENGLISH/geonet_english.html.

REFERENCES

Agnew, D.C., 1992. The time-domain behavior of power-law noises, *Geophys. Res. Lett.,* **19**(4), 333–336.

Agnew, D.C., 2013. Realistic simulations of geodetic network data: the Fakenet package, *Seismol. Res. Lett.,* **84**(3), 426–432.

Amiri-Simkooei, A.R., Tiberius, C.C. & Teunissen, P.J., 2007. Assessment of noise in GPS coordinate time series: methodology and results, *J. geophys. Res.: Solid Earth,* **112**(B7). doi: 10.1029/2006JB004913.

Anastasiou, A. & Fryzlewicz, P., 2022. Detecting multiple generalized change-points by isolating single ones, *Metrika,* **85**(2), 141–174.

Baba, T., Cummins, P.R., Hori, T. & Kaneda, Y., 2006. High precision slip distribution of the 1944 Tonankai earthquake inferred from tsunami waveforms: possible slip on a splay fault, *Tectonophysics,* **426**(1–2), 119–134.

Bagnardi, M. & Hooper, A., 2018. Inversion of surface deformation data for rapid estimates of source parameters and uncertainties: a Bayesian approach, *Geochem. Geophys. Geosyst.,* **19**(7), 2194–2211.

Barbot, S., 2019. Slow-slip, slow earthquakes, period-two cycles, full and partial ruptures, and deterministic chaos in a single asperity fault, *Tectonophysics,* **768,** 228171.

Bartlow, N.M., Wallace, L.M., Beavan, R.J., Bannister, S. & Segall, P., 2014. Time-dependent modeling of slow slip events and associated seismicity and tremor at the Hikurangi subduction zone, New Zealand, *J. geophys. Res.: Solid Earth,* **119**(1), 734–753.

Bedford, J. & Bevis, M., 2018. Greedy automatic signal decomposition and its application to daily GPS time series, *J. geophys. Res.: Solid Earth,* **123**(8), 6992–7003.

Beeler, N.M., Roeloffs, E. & McCausland, W., 2014. Re-estimated effects of deep episodic slip on the occurrence and probability of great earthquakes in cascadia, *Bull. seism. Soc. Am.,* **104**(1), 128–144.

Bletery, Q. & Nocquet, J.M., 2020. Slip bursts during coalescence of slow slip events in Cascadia, *Nat. Commun.,* **11**(1), 1–6.

Bormann, P. & Di Giacomo, D., 2011. The moment magnitude M_w and the energy magnitude M_e: common roots and differences, *J. Seismol.,* **15,** 2, 411–427.

Bos, M., Fernandes, R., Williams, S. & Bastos, L., 2013. Fast error analysis of continuous GNSS observations with missing data, *J. Geod.,* **87**(4), 351–360.

Bos, M.S., Montillet, J.P., Williams, S.D.P. & Fernandes, R.M.S., 2020. Introduction to geodetic time series analysis, in *Geodetic Time Series Analysis in Earth Sciences,* pp. 29–52, eds Montillet, J.-P. & Bos, M.S., Springer International Publishing.

Cavalié, O., Pathier, E., Radiguet, M., Vergnolle, M., Cotte, N., Walpersdorf, A., Kostoglodov, V. & Cotton, F., 2013. Slow slip event in the Mexican subduction zone: evidence of shallower slip in the Guerrero seismic gap for the 2006 event revealed by the joint inversion of INSAR and GPS data, *Earth planet. Sci. Lett.,* **367,** 52–60.

Chen, Q., van Dam, T., Sneeuw, N., Collilieux, X., Weigelt, M. & Rebischung, P., 2013. Singular spectrum analysis for modeling seasonal signals from GPS time series, *J. Geodyn.,* **72,** 25–35.

Costantino, G., Giffard-Roisin, S., Radiguet, M., Dalla Mura, M., Marsan, D. & Socquet, A., 2023. Multi-station deep learning on geodetic time series detects slow slip events in cascadia, *Commun. Earth Environ.,* **4**(1), 435.

Crowell, B.W., Bock, Y. & Liu, Z., 2016. Single-station automated detection of transient deformation in GPS time series with the relative strength index: a case study of Cascadian slow slip, *J. geophys. Res.: Solid Earth,* **121**(12), 9077–9094.

Davis, J.L., Wernicke, B.P. & Tamisiea, M.E., 2012. On seasonal signals in geodetic time series, *J. geophys. Res.: Solid Earth,* **117**(B1). doi: 10.1029/2011JB008690.

Dmitrieva, K., Segall, P. & DeMets, C., 2015. Network-based estimation of time-dependent noise in GPS position time series, *J. Geod.,* **89**(6), 591–606.

Dong, D., Fang, P., Bock, Y., Webb, F., Prawirodirdjo, L., Kedar, S. & Jamason, P., 2006. Spatiotemporal filtering using principal component analysis and Karhunen-loeve expansion approaches for regional GPS network analysis, *J. geophys. Res.: Solid Earth,* **111**(B3). doi: 10.1029/2005JB003806.

Donoso, F., nez, V.Y., Ortega-Culaciati, F. & Moreno, M., 2023. A machine learning approach for slow slip event detection using GNSS time-series, *J. South Am. Earth Sci.,* **132,** 104680.

ElGharbawi, T. & Tamura, M., 2015. Coseismic and postseismic deformation estimation of the 2011 Tohoku earthquake in Kanto region, Japan, using INSAR time series analysis and GPS, *Remote Sens. Environ.,* **168,** 374–387.

Fryzlewicz, P., 2014. Wild binary segmentation for multiple change-point detection, *Ann. Stat.,* **42**(6), 2243–2281.

Fujita, M., Nishimura, T. & Miyazaki, S., 2019. Detection of small crustal deformation caused by slow slip events in southwest Japan using GNSS and tremor data, *Earth Planets Space,* **71**(1), 1–13.

Fukuda, J., Higuchi, T., Miyazaki, S. & Kato, T., 2004. A new approach to time-dependent inversion of geodetic data using a Monte Carlo mixture Kalman filter, *Geophys. J. Int.,* **159**(1), 17–39.

Fukuda, J., Miyazaki, S., Higuchi, T. & Kato, T., 2008. Geodetic inversion for space—time distribution of fault slip with time-varying smoothing regularization, *Geophys. J. Int.,* **173**(1), 25–48.

Gazeaux, J. *et al.*, 2013. Detecting offsets in gps time series: First results from the detection of offsets in gps experiment, *J. geophys. Res.: Solid Earth,* **118**(5), 2397–2407.

Ghil, M. *et al.*, 2002. Advanced spectral methods for climatic time series, *Rev. Geophys.,* **40**(1), 3–1.

Granat, R., Parker, J., Kedar, S., Dong, D., Tang, B. & Bock, Y., 2013. Statistical approaches to detecting transient signals in GPS: results from the 2009–2011 transient detection exercise, *Seismol. Res. Lett.,* **84**(3), 444–454.

Hackl, M., Malservisi, R., Hugentobler, U. & Wonnacott, R., 2011. Estimation of velocity uncertainties from GPS time series: examples from the analysis of the South African Trignet Network, *J. geophys. Res.: Solid Earth,* **116**(B11). doi: 10.1029/2010JB008142.

Haines, J., Wallace, L.M. & Dimitrova, L., 2019. Slow slip event detection in Cascadia using vertical derivatives of horizontal stress rates, *J. geophys. Res.: Solid Earth,* **124**(5), 5153–5173.

He, X., Montillet, J.P., Fernandes, R., Bos, M., Yu, K., Hua, X. & Jiang, W., 2017. Review of current GPS methodologies for producing accurate time series and their error sources, *J. Geodyn.,* **106,** 12–29.

Hirose, H. & Kimura, T., 2020. Slip distributions of short-term slow slip events in Shikoku, southwest Japan, from 2001 to 2019 based on tilt change measurements, *J. geophys. Res.: Solid Earth,* **125**(6), e2020JB019601.

Hirose, H. & Obara, K., 2010. Recurrence behavior of short-term slow slip and correlated nonvolcanic tremor episodes in western Shikoku, southwest Japan, *J. geophys. Res.: Solid Earth,* **115**(B6). doi: 10.1029/2008JB006050.

Hirose, H., Hirahara, K., Kimata, F., Fujii, N. & Miyazaki, S., 1999. A slow thrust slip event following the two 1996 Hyuganada earthquakes beneath the Bungo channel, southwest Japan, *Geophys. Res. Lett.,* **26**(21), 3237–3240.

Hirose, H., Kimura, H., Enescu, B. & Aoi, S., 2012. Recurrent slow slip event likely hastened by the 2011 Tohoku earthquake, *Proc. Natl Acad. Sci.,* **109**(38), 15157–15161.

Ikari, M.J., Marone, C., Saffer, D.M. & Kopf, A.J., 2013. Slip weakening as a mechanism for slow earthquakes, *Nat. Geosci.,* **6**(6), 468–472.

Ito, Y. *et al.*, 2013. Episodic slow slip events in the Japan subduction zone before the 2011 Tohoku-Oki earthquake, *Tectonophysics,* **600,** 14–26.

Ito, Y., Obara, K., Shiomi, K., Sekine, S. & Hirose, H., 2007. Slow earthquakes coincident with episodic tremors and slow slip events, *Science,* **315**(5811), 503–506.

Ji, K., Shen, Y., Wang, F. & Chen, Q., 2024. An efficient improved singular spectrum analysis for processing GNSS position time series with missing data, *Geophys. J. Int.,* **240**(1), 189–200.

Ji, K.H. & Herring, T.A., 2013. A method for detecting transient signals in GPS position time-series: smoothing and principal component analysis, *Geophys. J. Int.,* **193**(1), 171–186.

Jiang, Y., Wdowinski, S., Dixon, T.H., Hackl, M., Protti, M. & Gonzalez, V., 2012. Slow slip events in Costa Rica detected by continuous GPS observations, 2002–2011, *Geochem. Geophys. Geosyst.,* **13**(4). doi: 10.1029/2012GC004058.

Jordan, T.H. & Jones, L.M., 2010. Operational earthquake forecasting: some thoughts on why and how, *Seismol. Res. Lett.,* **81**(4), 571–574.

Kano, M. & Kato, A., 2020. Detailed spatial slip distribution for short-term slow slip events along the Nankai subduction zone, southwest Japan, *J. geophys. Res.: Solid Earth,* **125**(7), e2020JB019613.

Kano, M. *et al.*, 2018. Development of a slow earthquake database, *Seismol. Res. Lett.,* **89**(4), 1566–1575.

Kobayashi, A., 2010. A small scale long-term slow slip occurred in the western Shikoku in 2005, *Zisin (Journal of the Seismological Society of Japan. 2nd ser.),* **63**(2), 97–100.

Kobayashi, A., 2012. Long-term slow slip event around Kochi city from 1977 to 1980, *Zisin (Journal of the Seismological Society of Japan. 2nd ser.),* **64**(2), 63–73.

Langbein, J. & Svarc, J.L., 2019. Evaluation of temporally correlated noise in global navigation satellite system time series: Geodetic monument performance, *J. geophys. Res.: Solid Earth,* **124**(1), 925–942.

Liu, J., Wu, S. & Zidek, J.V., 1997. On segmented multivariate regression, *Stat. Sin.,* **7,** 497–525. https://www.jstor.org/stable/24306090.

Lohman, R.B. & Murray, J.R., 2013. The SCEC geodetic transient detection validation exercise, *Seismol. Res. Lett.,* **84**(3), 419–425.

Ma, Y.M.(2025). SSAID: An R package for automated detection of short-term slow slip events using GNSS data via change-point analysis. In Geophysical Journal International. Zenodo. https://doi.org/10.5281/zenodo.18038709.

Mao, A., Harrison, C.G. & Dixon, T.H., 1999. Noise in GPS coordinate time series, *J. geophys. Res.: Solid Earth,* **104**(B2), 2797–2816.

Mazzotti, S. & Adams, J., 2004. Variability of near-term probability for the next great earthquake on the Cascadia subduction zone, *Bull. seism. Soc. Am.,* **94**(5), 1954–1959.

McCaffrey, R., 2009. Time-dependent inversion of three-component continuous GPS for steady and transient sources in northern Cascadia, *Geophys. Res. Lett.,* **36**(7). doi: 10.1029/2008GL036784.

McGuire, J.J. & Segall, P., 2003. Imaging of aseismic fault slip transients recorded by dense geodetic networks, *Geophys. J. Int.,* **155**(3), 778–788.

Melbourne, T.I., Szeliga, W.M., Miller, M.M. & Santillan, V.M., 2005. Extent and duration of the 2003 Cascadia slow earthquake, *Geophys. Res. Lett.,* **32**(4). doi: 10.1029/2004GL021790.

Miyazaki, S. & Heki, K., 2001. Crustal velocity field of southwest japan: Subduction and arc-arc collision, *J. geophys. Res.: Solid Earth,* **106**(B3), 4305–4326.

Miyazaki, S., McGuire, J.J. & Segall, P., 2003. A transient subduction zone slip episode in southwest Japan observed by the nationwide GPS array, *J. geophys. Res.: Solid Earth,* **108**(B2). doi: 10.1029/2001JB000456.

Nikolaidis, R., 2002. *Observation of geodetic and seismic deformation with the Global Positioning System, PhD thesis,* University of California, San Diego.

Nishikawa, T., Matsuzawa, T., Ohta, K., Uchida, N., Nishimura, T. & Ide, S., 2019. The slow earthquake spectrum in the Japan trench illuminated by the s-net seafloor observatories, *Science,* **365**(6455), 808–813.

Nishimura, T., 2014. Short-term slow slip events along the Ryukyu trench, southwestern Japan, observed by continuous GNSS, *Progr. Earth Planet. Sci.,* **1**(1), 1–13.

Nishimura, T., 2021. Slow slip events in the Kanto and Tokai regions of central Japan detected using global navigation satellite system data during 1994–2020, *Geochem. Geophys. Geosyst.,* **22**(2), e2020GC009329.

Nishimura, T., Matsuzawa, T. & Obara, K., 2013. Detection of short-term slow slip events along the Nankai trough, southwest Japan, using GNSS data, *J. geophys. Res.: Solid Earth,* **118**(6), 3112–3125.

Obara, K. & Kato, A., 2016. Connecting slow earthquakes to huge earthquakes, *Science,* **353**(6296), 253–257.

Obara, K., 2020. Characteristic activities of slow earthquakes in Japan, *Proc. Japan Acad. Ser. B,* **96**(7), 297–315.

Obara, K., Tanaka, S., Maeda, T. & Matsuzawa, T., 2010. Depth-dependent activity of non-volcanic tremor in southwest Japan, *Geophys. Res. Lett.,* **37**(13). doi: 10.1029/2010GL043679.

Ohtani, R., McGuire, J.J. & Segall, P., 2010. Network strain filter: a new tool for monitoring and detecting transient deformation signals in GPS arrays, *J. geophys. Res.: Solid Earth,* **115**(B12). doi: 10.1029/2010JB007442.

Okada, Y., 1985. Surface deformation due to shear and tensile faults in a half-space, *Bull. seism. Soc. Am.,* **75**(4), 1135–1154.

Okada, Y., Nishimura, T., Tabei, T., Matsushima, T. & Hirose, H., 2022. Development of a detection method for short-term slow slip events using GNSS data and its application to the Nankai subduction zone, *Earth Planets Space,* **74**(1), 1–18.

Olivares-Pulido, G., Teferle, F.N. & Hunegnaw, A., 2020. Markov chain Monte Carlo and the application to geodetic time series analysis, in *Geodetic Time Series Analysis in Earth Sciences,* pp. 53–138, eds Montillet, J.-P. & Bos, M.S., Springer International Publishing.

Olivares, G. & Teferle, N., 2013. A Bayesian Monte Carlo Markov Chain method for the analysis of GPS position time series, in *EGU General Assembly Conference Abstracts,* Vienna, Austria, pp. EGU2013–10497.

Ozawa, S.W., Hatano, T. & Kame, N., 2019. Longer migration and spontaneous decay of aseismic slip pulse caused by fault roughness, *Geophys. Res. Lett.,* **46**(2), 636–643.

Radiguet, M. *et al.*, 2016. Triggering of the 2014 M_w7. 3 Papanoa earthquake by a slow slip event in Guerrero, Mexico, *Nat. Geosci.,* **9**(11), 829–833.

Riel, B., Simons, M., Agram, P. & Zhan, Z., 2014. Detecting transient signals in geodetic time series using sparse estimation techniques, *J. geophys. Res.: Solid Earth,* **119**(6), 5140–5160.

Rogers, G. & Dragert, H., 2003. Episodic tremor and slip on the Cascadia subduction zone: the chatter of silent slip, *Science,* **300**(5627), 1942–1943.

Rousset, B., Campillo, M., Lasserre, C., Frank, W.B., Cotte, N., Walpersdorf, A., Socquet, A. & Kostoglodov, V., 2017. A geodetic matched filter search for slow slip with application to the Mexico subduction zone, *J. geophys. Res.: Solid Earth,* **122**(12), 10498–10514.

Saffer, D.M. & Wallace, L.M., 2015. The frictional, hydrologic, metamorphic and thermal habitat of shallow slow earthquakes, *Nat. Geosci.,* **8**(8), 594–600.

Sagiya, T. & Thatcher, W., 1999. Coseismic slip resolution along a plate boundary megathrust: the Nankai trough, southwest japan, *J. geophys. Res.: Solid Earth,* **104**(B1), 1111–1129.

Segall, P. & Matthews, M., 1997. Time dependent inversion of geodetic data, *J. geophys. Res.: Solid Earth,* **102**(B10), 22391–22409.

Segall, P., Bürgmann, R. & Matthews, M., 2000. Time-dependent triggered afterslip following the 1989 Loma Prieta earthquake, *J. geophys. Res.: Solid Earth,* **105**(B3), 5615–5634.

Segall, P., Desmarais, E.K., Shelly, D., Miklius, A. & Cervelli, P., 2006. Earthquakes triggered by silent slip events on kīlauea volcano, hawaii, *Nature,* **442**(7098), 71–74.

Shiomi, K., Matsubara, M., Ito, Y. & Obara, K., 2008. Simple relationship between seismic activity along Philippine sea slab and geometry of oceanic moho beneath southwest Japan, *Geophys. J. Int.,* **173**(3), 1018–1029.

Smith, E.F. & Gomberg, J., 2009. A search in strainmeter data for slow slip associated with triggered and ambient tremor near Parkfield, California, *J. geophys. Res.: Solid Earth,* **114**(B12). doi: 10.1029/2008JB006040.

Takagi, R., Uchida, N. & Obara, K., 2019. Along-strike variation and migration of long-term slow slip events in the western Nankai subduction zone, Japan, *J. geophys. Res.: Solid Earth,* **124**(4), 3853–3880.

Tan, W., Chen, J., Zhang, Y., Wang, B. & Wang, S., 2024. Singular spectrum analysis for the time-variable seasonal signals from GPS in Yunnan province, *Geod. Geodyn.,* **15**(6), 582–591.

Vautard, R., Yiou, P. & Ghil, M., 1992. Singular-spectrum analysis: a toolkit for short, noisy chaotic signals, *Phys. D: Nonlin. Phenomena,* **58**(1-4), 95–126.

Vergnolle, M., Walpersdorf, A., Kostoglodov, V., Tregoning, P., Santiago, J., Cotte, N. & Franco, S., 2010. Slow slip events in Mexico revised from the processing of 11 year GPS observations, *J. geophys. Res.: Solid Earth,* **115**(B8). doi: 10.1029/2009JB006852.

Voss, N., Dixon, T.H., Liu, Z., Malservisi, R., Protti, M. & Schwartz, S., 2018. Do slow slip events trigger large and great megathrust earthquakes?, *Sci. Adv.,* **4**(10), eaat8472. doi: 10.1126/sciadv.aat8472.

Wallace, L.M., 2020. Slow slip events in New Zealand, *Annu. Rev. Earth planet. Sci.,* **48,** 1, 175–203.

Wallace, L.M., Hreinsdóttir, S., Ellis, S., Hamling, I., D'Anastasio, E. & Denys, P., 2018. Triggered slow slip and afterslip on the southern Hikurangi subduction zone following the Kaikōura earthquake, *Geophys. Res. Lett.,* **45**(10), 4710–4718.

Wallace, L.M., Kaneko, Y., Hreinsdóttir, S., Hamling, I., Peng, Z., Bartlow, N., D'Anastasio, E. & Fry, B., 2017. Large-scale dynamic triggering of shallow slow slip enhanced by overlying sedimentary wedge, *Nat. Geosci.,* **10**(10), 765–770.

Walwer, D., Calais, E. & Ghil, M., 2016. Data-adaptive detection of transient deformation in geodetic networks, *J. geophys. Res.: Solid Earth,* **121**(3), 2129–2152.

Wang, T., Zhuang, J., Buckby, J., Obara, K. & Tsuruoka, H., 2018. Identifying the recurrence patterns of nonvolcanic tremors using a 2-D hidden Markov model with extra zeros, *J. geophys. Res.: Solid Earth,* **123**(8), 6802–6825.

Wdowinski, S., Bock, Y., Zhang, J., Fang, P. & Genrich, J., 1997. Southern california permanent GPS geodetic array: spatial filtering of daily positions for estimating coseismic and postseismic displacements induced by the 1992 landers earthquake, *J. geophys. Res.: Solid Earth,* **102**(B8), 18 057–18 070.

Williams, C.A. & Wallace, L.M., 2015. Effects of material property variations on slip estimates for subduction interface slow-slip events, *Geophys. Res. Lett.,* **42**(4), 1113–1121.

Williams, S.D., Bock, Y., Fang, P., Jamason, P., Nikolaidis, R.M., Prawirodirdjo, L., Miller, M. & Johnson, D.J., 2004. Error analysis of continuous GPS position time series, *J. geophys. Res.: Solid Earth,* **109**(B3), doi: 10.1029/2003JB002741.

Xue, X. & Freymueller, J.T., 2023. Machine learning for single-station detection of 0258 transient deformation in GPS time series with a case study of Cascadia slow slip, *J. geophys. Res.: Solid Earth,* **128**(2), e2022JB024859.

Yagi, Y., 1998. Source process of the Hyuga-nada earthquake of April 1, 1968 ($M_{\rm JMA}$ 7.5), and its relationship to the subsequent seismicity, *Zisin,* **51**(1), 139–148.

Yano, K. & Kano, M., 2022. L1 trend filtering-based detection of short-term slow slip events: application to a GNSS array in southwest Japan, *J. geophys. Res.: Solid Earth,* **127**(5), e2021JB023258.

Yao, Y.C., 1988. Estimating the number of change-points via Schwarz'criterion, *Stat. Probab. Lett.,* **6**(3), 181–189.

Yarai, H. & Ozawa, S., 2013. Quasi-periodic slow slip events in the afterslip area of the 1996 Hyuga-Nada earthquakes, Japan, *J. geophys. Res.: Solid Earth,* **118**(5), 2512–2527.

Zhang, J., Bock, Y., Johnson, H., Fang, P., Williams, S., Genrich, J., Wdowinski, S. & Behr, J., 1997. Southern California permanent GPS geodetic array: error analysis of daily position estimates and site velocities, *J. geophys. Res.: solid earth,* **102**(B8), 18 035–18 055.

SUPPORTING INFORMATION

Supplementary data are available at *GJIRAS* online.

suppl_data

Please note: Oxford University Press is not responsible for the content or functionality of any supporting materials supplied by the authors. Any queries (other than missing material) should be directed to the corresponding author for the paper.

APPENDIX A: METHODOLOGY OF SSAID

SSAID is roughly divided into four steps, as shown in Fig. 2: (1) decomposing the input data into different components by singular spectrum analysis (SSA) and then reconstructing data with different noise levels; (2) adding independent Gaussian noise with various noise levels back to each reconstructed signal to generate new noisy data, some of which are in-SNL data; (3) identifying in-SNL data from the new noisy data generated in Step 2; (4) outputting the locations of estimated change-points for the input data. The pseudocode of SSAID can be found in the supplement (see Section S8).

A1 Step 1: Decomposition process

SSA is a powerful non-parametric tool for separating underlying signals from the noise, without the need of *a priori* knowledge of the underlying dynamics (M. Ghil *et al.* 2002; Q. Chen *et al.* 2013; D. Walwer *et al.* 2016; K. Ji *et al.* 2024; W. Tan *et al.* 2024). However, it is not designed for detecting change-points. SSA decomposes the noisy data into different components, and then chooses some of these components in order to reconstruct the signal for the underlying true dynamics. We first use SSA to decompose X_t into M components, $X_t = \sum_{j=1}^{M} R_t^j$, each R_t^j $(j = 1, \cdots, M)$ denoting an oscillatory component. We then create M sequences of data Y_t by

$$Y_t^k = \sum_{j=1}^{k} R_t^j \quad (k = 1, \cdots, M; t = 1, \cdots, T). \tag{A1}$$

The components R_t^j $(j = 1, \cdots, M)$ are sorted in a decreasing order according to their correlation with the underlying dynamics. That is, R_t^j with smaller j are important components of the underlying signal, while those with larger j mostly contain noise. Therefore, the noise level in Y_t^k increases with k, such that $Y_t^M = X_t$, that is, no information is lost by this decomposition process. If the noise level in the input data is lower than its minimum SNL, the noise levels for all Y_t^k, $k < M$, are also lower than its minimum SNL. Even if the noise level of the input data is large enough to incorporate the SNL range, it is still possible that all the generated Y_t^k do not have an SNL, since the noise level of these Y_t^k is increasing with k at uneven intervals. Therefore, this decomposition cannot ensure the existence of in-SNL data; this is the reason why Step 2 below needs to be implemented in the proposed method.

A2 Step 2: Adding extra noise

After Step 1, we construct L new sequences of noisy data $Z_t^{k,s}$ for each denoised signal Y_t^k $(k = 1, \cdots, M)$ to ensure that some in-SNL data can be obtained as follows,

$$Z_t^{k,s} = Y_t^k + a_s \omega_t \quad (k = 1, \cdots, M; s = 1, \cdots, L; t = 1, \cdots, T), \tag{A2}$$

where ω_t are independent standard, Gaussian random variables and a_s is the level of added noise. If Y_t^k has an SNL and a_s is small enough, $Z_t^{k,s}$ should still have an SNL. Conversely, if Y_t^k has a noise level lower than its minimum SNL and a_s is large enough, $Z_t^{k,s}$ can have an SNL. Therefore, the level of added noise a_s must vary over a sufficiently large range to ensure that some $Z_t^{k,s}$ have an SNL.

Once we obtain in-SNL data, the existing CPD methods for continuous piecewise-linear signals can be applied to detect their change-points (see the tests in the supplement), where we also showed that the percentage of successful cumulative detections $R_{\rm sd}$ (see eq. (3)) is never higher than $70 - 80$ per cent [see Fig. S4(b) in the supplement], even when the analysed signal has noise in the SNL range. Consequently, we refrain from directly applying the existing CPD methods to these new sequences of noisy data $Z_t^{k,s}$. Instead, we implement an enhancement scheme to increase the percentage of successful cumulative detection $R_{\rm sd}$ for in-SNL data.

In this enhancement scheme, we follow the procedure below to increase $R_{\rm sd}$ for in-SNL data. (1) We generate Q realizations of the time-series in eq. (A2), and we denote these by $Z_t^{k,s,m} = Y_t^k + a_s \omega_t^m$ $(m = 1, \cdots, Q)$, where ω_t^m is the m-th realization of the noise ω_t in eq. (A2). That is, for the same noise level a_s, ω_t is simulated Q times. The Q realizations of $Z_t^{k,s}$ are collected in a set $\boldsymbol{G}^{k,s} = \{Z_t^{k,s,1}, \cdots, Z_t^{k,s,Q}\}$. For ease of presentation, this set $\boldsymbol{G}^{k,s}$

is called a group. Every realization $Z_t^{k,s,m}$ in this group is called a member and has the same noise level as $Z_t^{k,s}$ (see Step 3 in Fig. 2). (2) The change-points in each $Z_t^{k,s,m}$ are detected by a chosen CPD method for continuous piecewise-linear signals. Here, we use the ID method of A. Anastasiou & P. Fryzlewicz (2022) as it is the only one among the five methods examined in Section S3 in the supplement that exhibits an SNL range for all the simulated SSEs in spite of the number of change-points (see Fig. S9 in the supplement). (3) We determine $\hat{N}^{k,s}$, the number of estimated change-points in $Z_t^{k,s}$, and identify the locations of the estimated change-points in $Z_t^{k,s}$, stored in a vector $\boldsymbol{U}^{k,s}$. Further elaborations on the third procedure can be found in the subsequent two paragraphs.

First, we determine $\hat{N}^{k,s}$ by a majority voting rule based on the following results. Let F denote the number of realizations in $\boldsymbol{G}^{k,s}$ with successful cumulative detections (see the definition of a successful cumulative detection in Section 2). Let P_s be the probability that a cumulative detection is successful for a given noise level a_s. As $Z_t^{k,s,m}(m = 1, \cdots, Q)$ are independent of each other, the probability that at least half of these cumulative detections in group $\boldsymbol{G}^{k,s}$ are successful is

$$P\left(F \geq \frac{Q}{2}\right) = \sum_{q=\lceil Q/2 \rceil}^{Q} P\,(F = q) = \sum_{q=\lceil Q/2 \rceil}^{Q} \binom{Q}{q} P_s^q (1 - P_s)^{Q-q}. \tag{A3}$$

According to the Law of Large Numbers, when the sample size Q is sufficiently large (i.e. $Q \to \infty$), the relative proportion $\frac{F}{Q}$ converges to the probability of success P_s (i.e. $\lim_{Q\to\infty} \frac{F}{Q} = P_s$), If $Z_t^{k,s}$ is an in-SNL data, by the definition of the SNL in Section 2, P_s is over 0.5, hence $P\,(F \geq Q/2)$ will converge to 1 if Q is large enough. For example, $P\,(F \geq Q/2)$ is 0.9832 if $P_s = 0.6$ and $Q = 100$. Thus, we can estimate the number of change-points for $Z_t^{k,s}$ by using the mode of the $\hat{N}^{k,s,m}$ values, denoted by $\hat{N}^{k,s} = Mo\{\hat{N}^{k,s,1}, \cdots, \hat{N}^{k,s,Q}\}$, where $\hat{N}^{k,s,m}$ is the number of estimated change-points for $Z_t^{k,s,m}$ and $Mo\{\cdot\}$ denotes the mode. According to eq. (A3), the probability that $\hat{N}^{k,s}$ is equal to the number of true change-points in $Z_t^{k,s}$ is close to 1, if $Z_t^{k,s}$ is an in-SNL data.

Secondly, we identify the locations of estimated change-points for $Z_t^{k,s}$. For ease of discussion, we call a member of $G^{k,s}$ a qualified member if it satisfies $\hat{N}^{k,s,m} = \hat{N}^{k,s}$. Let κ denote the number of qualified members in group $G^{k,s}$. The locations of the estimated change-points for the j-th qualified member are collected in a vector $u^{k,s,j}$. All these $u^{k,s,j}$ have the same length; this being $\hat{N}^{k,s}$. We store these vectors into a matrix

$$D = \begin{pmatrix} \hat{\theta}_{1,1} & \hat{\theta}_{1,2} & \cdots & \hat{\theta}_{1,\hat{N}^{k,s}} \\ \vdots & \vdots & \vdots & \vdots \\ \hat{\theta}_{j,1} & \hat{\theta}_{j,2} & \cdots & \hat{\theta}_{j,\hat{N}^{k,s}} \\ \vdots & \vdots & \vdots & \vdots \\ \hat{\theta}_{\kappa,1} & \hat{\theta}_{\kappa,2} & \cdots & \hat{\theta}_{\kappa,\hat{N}^{k,s}} \end{pmatrix}, \tag{A4}$$

where $\hat{\theta}_{j,i}$ is the location of the i-th estimated change-point for the j-th qualified member, that is, $u^{k,s,j} = \{\hat{\theta}_{j,1}, \cdots, \hat{\theta}_{j,\hat{N}^{k,s}}\}$, $j = 1, \cdots, \kappa$. We take the mode of the i-th column in D as the estimated location of the i-th change-point for $Z_t^{k,s}$, denoted by $U_i^{k,s} = Mo\{\hat{\theta}_{1,i}, \cdots, \hat{\theta}_{\kappa,i}\}, i = 1, \cdots, \hat{N}^{k,s}$. Therefore, the estimated change-point locations for $Z_t^{k,s}$ are $U^{k,s} = \{U_1^{k,s}, \cdots, U_{\hat{N}^{k,s}}^{k,s}\}$.

We confirm that the proposed majority voting rule above can significantly increase the percentage of successful cumulative detections R_{sd} to 100 per cent, when the input data has an SNL, by numerical tests (see Section S4 in the supplement).

A3 Step 3: Identifying in-SNL data

After adding noise, we have generated $L \times M \times Q$ new noisy data $Z_t^{k,s,m}(k = 1, \cdots, M; s = 1, \cdots, L; m = 1, \cdots, Q)$ (see Step 3 in Fig. 2) to produce in-SNL data from the input data. However, only some of these noisy data are in-SNL data. Based on the tests conducted in Section S3 in the supplement, we impose three conditions observed to identify in-SNL data: (1) $R_2 \geq 50$ per cent, (2) $\hat{N} \neq 0$ and (3) $\Omega_3 \leq v$. Here, $R_2 \geq 50$ per cent refers to the percentage of qualified members (see the definition in Section A2, i.e. $\hat{N}^{k,s,m} = \hat{N}^{k,s}$) in a given group (i.e. $R_2 = \kappa/Q$), $\hat{N}$ is the number of estimated change-points for each group by taking its mode (also see the definition of $\hat{N}$ for each group in Section A2), Ω_3 is the third quartile of the RMSE calculated for each group and v is a predefined threshold to define a successful cumulative detection (see Section 2, i.e. $v = 3$ for these simulated SSE data). The aim of the first condition is to locate in-SNL data. However, $R_2 \geq 50$ per cent can occur when the noise level is an SNL or when it is much larger than the SNL range, for which the number of estimated change-points $\hat{N} = 0$. This situation is demonstrated in Fig. S11(a) (see the cyan areas) in the supplement. The second condition remedies this pathology. Finally, the third condition aims to remove groups with low accuracy. When calculating the RMSE, the locations of true change-points in the real-world data is estimated through the approach shown in eq. (A4). Members of a group for which the three conditions are met are all in-SNL data. Otherwise, none of them is. For cases in which no change-points are present in the input data X_t, no groups have in-SNL data since $\hat{N} = 0$, which means that SSAID will not output any change-points (i.e. $\hat{N} = 0$). The quantities $R_2^{k,s}$, $\hat{N}^{k,s}$ and $\Omega_3^{k,s}$ indicated in Fig. 2 (see Step 3) are R_2, $\hat{N}$ and Ω_3 for group $\boldsymbol{G}^{k,s}$, respectively.

A4 Step 4: Outputting the final change-points

We now estimate the locations of change-points in the raw data X_t based on the identified in-SNL data. First, we compute the mode of the distribution of detected change-points in all the identified in-SNL data as the number of estimated change-points $\hat{N}_X$ in the raw data X_t. If no non-zero $\hat{N}_X$ value is found, it indicates that SSAID did not detect any change-points in the input data X_t, and SSAID outputs no change-points without proceeding further. However, once a non-zero $\hat{N}_X$ is identified, we move to the next step.

Next, we collect the estimated change-points from the in-SNL data that have the same number of change-points as $\hat{N}_X$ into a matrix D_f, where each row of D_f represents the locations of detected change-points for a corresponding in-SNL data sequence. Then, we generate two candidate sets of final change-points in X_t by calculating both the mode and the average for each column of D_f. Finally, the sSIC criterion is used to select the set of change-points that best characterizes the input data.